Journal of Geophysical Research: Oceans

RESEARCH ARTICLE
10.1029/2018JC013769

Special Section:
Sea State and Boundary Layer Physics of the Emerging Arctic Ocean

Arctic Sea Ice Drift Measured by Shipboard Marine Radar

B. Lund[1,2], H. C. Graber[1,2], P. O. G. Persson[3], M. Smith[4], M. Doble[5], J. Thomson[4], and P. Wadhams[6]

[1]Department of Ocean Sciences, Rosenstiel School of Marine and Atmospheric Science, University of Miami, Miami, FL, USA, [2]Center for Southeastern Tropical Advanced Remote Sensing, University of Miami, Miami, FL, USA, [3]ESRL Physical Sciences Division, National Oceanic and Atmospheric Administration, Boulder, CO, USA, [4]Applied Physics Laboratory, University of Washington, Seattle, WA, USA, [5]Polar Scientific Limited, Dallens, Appin, United Kingdom, [6]Department of Applied Mathematics and Theoretical Physics, Cambridge University, Cambridge, United Kingdom

Abstract This study presents Arctic sea ice drift fields measured by shipboard marine X-band radar (MR). The measurements are based on the maximum cross correlation between two sequential MR backscatter images separated ~1 min in time, a method that is commonly used to estimate sea ice drift from satellite products. The advantage of MR is that images in close temporal proximity are readily available. A typical MR antenna rotation period is ~1–2 s, whereas satellite revisit times can be on the order of days. The technique is applied to ~4 weeks of measurements taken from R/V *Sikuliaq* in the Beaufort Sea in the fall of 2015. The resulting sea ice velocity fields have ~500 m and up to ~5 min resolution, covering a maximum range of ~4 km. The MR velocity fields are validated using the GPS-tracked motion of Surface Wave Instrument Float with Tracking (SWIFT) drifters, wave buoys, and R/V *Sikuliaq* during ice stations. The comparison between MR and reference sea ice drift measurements yields root-mean-square errors from 0.8 to 5.6 cm s^{-1}. The MR sea ice velocity fields near the ice edge reveal strong horizontal gradients and peak speeds >1 m s^{-1}. The observed submesoscale sea ice drift processes include an eddy with ~6 km diameter and vorticities <-2 (normalized by the Coriolis frequency) as well as converging and diverging flow with normalized divergences <-2 and >1, respectively. The sea ice drift speed correlates only weakly with the wind speed ($r^2 = 0.34$), which presents a challenge to conventional wisdom.

Key Points:
- Marine X-band radar data are processed to yield sub-km scale sea ice velocity fields
- Root-mean-square errors between radar and reference sea ice drift measurements are ~1–6 cm ŝ–1
- Contrary to conventional wisdom, sea ice drift and wind speed are only weakly correlated ($\dot{r}2 = 0.34$) near the ice edge

Supporting Information:
- Supporting Information S1
- Movie S1

Correspondence to:
B. Lund,
blund@cstars.miami.edu

Citation:
Lund, B., Graber, H. C., Persson, P. O. G., Smith, M., Doble, M., Thomson, J., et al. (2018). Arctic sea ice drift measured by shipboard marine radar. *Journal of Geophysical Research: Oceans*, *123*. https://doi.org/10.1029/2018JC013769

Received 10 JAN 2018
Accepted 16 APR 2018
Accepted article online 19 APR 2018

1. Introduction

This study presents sea ice drift measurements that were made from a research vessel within the marginal ice zone (MIZ) of the fall Beaufort Sea. The MIZ connects the open ocean with the pack ice, extending over 150–200 km (Wadhams, 1980). It is characterized by a loose ice cover with large areas of open ocean. As a result, its ice has lower internal stress and greater freedom of movement than the central pack ice. The MIZ is furthermore influenced by surface waves that can penetrate into it and modify the characteristics of its ice, e.g., through breakup or pancake formation (e.g., Squire, 2007).

Sea ice drift measurements are crucial for understanding the air-sea-ice system in higher latitudes. Sea ice mediates the exchange of heat, mass, and momentum between atmosphere and ocean. Local sea ice drift divergences are likely to result in leads opening up. In winter, the sensible heat flux through leads is 10–100 times greater than that through sea ice (Ledley, 1988). In summer, open water absorbs over 90% of incoming solar radiation, whereas snow-covered ice reflects 80% (Smith et al., 1990). Sea ice drift convergences cause ridging and rafting, affecting local sea ice thicknesses. Sea ice reduces upper ocean stability during freezing (through brine production) and increases stability during melting (by freshening the surface layer; Leppäranta, 2011). It also modifies the atmospheric boundary layer, and especially so in the MIZ, where the atmospheric flow encounters frequent and drastic changes in sea surface temperature and roughness (Andreas et al., 1984). Lastly, the ice edge location plays a key role for Arctic summer bioproductivity (Perrette et al., 2011).

Sea ice drift is controlled by the interplay of wind stress, ocean drag, and internal ice friction (e.g., Campbell, 1965). In the MIZ, where internal ice friction is typically negligible, simultaneous observations of sea ice drift, wind drag, and upper ocean currents could be used to derive ocean drag, which is difficult to measure

otherwise (Leppäranta, 2011). They may furthermore prove useful for validating high-resolution (∼1 km) regional sea ice models (e.g., Rousset et al., 2015). In addition to these scientific motivations, sea ice drift measurements from ships may be valuable in several practical applications. The Northern Sea Route and Northwest Passage connecting the North Atlantic and Asia are expected to grow in importance as the navigation season lengthens under a changing climate (Khon et al., 2010). Routine, near real-time sea ice drift data can aid navigation, e.g., by identifying local sea ice drift divergences (and associated leads). They can also be used for estimating sea ice loads on offshore structures (e.g., a wind turbine or oil drilling platform) and ships (Ponter et al., 1983). Finally, sea ice drift mapping capabilities onboard emergency response vessels will allow the tracking of pollutants like spilled oil and help mitigate associated risks, which are likely to increase as Arctic navigation and exploration expands (Jernelöv, 2010).

Satellite remote sensing has long been used to derive sea ice drift from pairs of sequential images. Early studies from the 1970s used visible images acquired by ERTS-1 which offer a spatial resolution of ∼1 km (Campbell et al., 1975; Nye, 1975). In these studies, the sea ice drift was determined manually by identifying ice floes that are present in both images and measuring the distances they traveled. The 1980s brought the advent of automated sea ice drift retrieval techniques. Emery et al. (1986) and Ninnis et al. (1986) achieved this by cross correlating sequential infrared and visible images acquired by AVHRR. Both visible and infrared sensors require cloud-free conditions, the former are furthermore limited to daylight hours. These limitations were overcome by synthetic aperture radar (SAR), which in addition offers finer spatial resolution (∼10–100 m). Numerous studies use SAR data for sea ice drift retrieval. The studies by Hall and Rothrock (1981) and Curlander et al. (1985), based on Seasat SAR imagery, still derive drift manually. But automatic retrieval has since become widespread, with Fily and Rothrock (1987) who use a cross-correlation technique and Vesecky et al. (1988) who use a feature tracking technique being among the first. The former employs Eulerian sampling (i.e., sea ice drift is computed at specific fixed locations) and the latter Lagrangian sampling (i.e., it yields trajectories for select ice floes). In the early 1990s, when SAR data from the ERS-1, JERS-1, and RADARSAT satellites became widely available, the scientific focus turned toward sea ice drift retrieval in operational settings (Holt et al., 1992; Kwok, 1998; Kwok et al., 1990). Since then, the cross-correlation technique has been improved (Sun, 1994) and a higher-resolution product has been obtained (Thomas et al., 2008). Today, while operational support (Karvonen, 2012) and quality control (Bouillon & Rampal, 2015; Lindsay & Stern, 2003) remain active research topics, SAR-based sea ice drift retrieval has developed into a mature research field.

On a significantly larger scale (spatial resolutions of 10 km or more), SMMR, SSM/I, and AMSR2 passive microwave data as well as SeaWinds, ASAT, and QuickSCAT scatterometer data have been used to produce coarse (∼100 km) sea ice velocity fields (Emery et al., 1997; Girard-Ardhuin & Ezraty, 2012; Haarpaintner, 2006; Spreen et al., 2008). Scatterometer and passive microwave sea ice velocity fields provide an excellent view of longer-term, larger-scale drift patterns, but are ill suited for the computation of short-term spatial derivatives like divergence or vorticity (Kwok, 2010; Kwok et al., 1998; Sumata et al., 2014). SAR-based velocity fields offer finer spatial resolution (∼5 km), providing insights on the ice cover's small-scale and time-varying deformation (Kwok, 2006). However, due to limits in swath widths and orbit repeat cycles, resolving ice drift trends at subdaily time scales remains out of reach with the existing satellite sensors.

The MIZ, with its spatially variable ice cover and associated strong gradients (e.g., in terms of mixed layer temperature and salinity), is subject to particularly strong air-sea-ice interactions and submesoscale (∼100 m to 10 km) upper ocean dynamics (Manucharyan & Thompson, 2017; McPhee et al., 1987; Timmermans et al., 2012). Given the continuous changes in the location of the ice edge and local ice concentration, characteristic time scales are likely on the order of hours. This study uses shipborne marine X-band radar (MR) data with a maximum range of 4 km and spatiotemporal resolution on the order of 10 m and 1 s. Hence, an ideal sensor for resolving the MIZ's submesoscale dynamics.

Several investigators have used coastal MRs for sea ice monitoring. In the late 1960s, a network of three coastal C-band radar stations (similar to weather radars) was constructed to monitor the pack ice off the coast of Hokkaido, Japan. Using data from this coastal radar network, Tabata (1975) proposes a sea ice drift retrieval technique based on cross correlation, and Tabata et al. (1980) investigate the ice pack's divergence and rotation. The C-band radars were replaced in 2004 by a HF radar network, which provides information on the location of the sea ice edge but not ice drift (Shirasawa et al., 2013). The earliest studies to employ coastal MRs focus on sea ice imaging, but also discuss the sea ice classification potential (i.e., distinguishing

between open water, first-year ice, multiyear ice, and icebergs; Flock, 1977; Haykin et al., 1985; Lewis et al., 1994; Shapiro & Metzner, 1989). More recently, a MR installed in Barrow, AK, has been used to study the attachment and detachment of nearshore ice (Druckenmiller et al., 2009; Mahoney et al., 2007). Using MR data from the same station, Rohith et al. (2013) developed a dense and feature-based optical flow technique to extract sea ice velocity fields, ice floe trajectories, and delineate the boundary of stable landfast ice. A first independent validation of their technique was carried out by Mahoney et al. (2015) using an under-ice acoustic Doppler current profiler (ADCP). Concurrently, as part of their operational sea ice monitoring, the Finnish Meteorological Institute (FMI) has installed two MRs along the Baltic Sea coast. Data from these systems have been used to develop sea ice drift retrieval techniques that are based on cross correlation (Karvonen et al., 2010), feature tracking combined with cross correlation (Karvonen, 2013), and feature tracking combined with optical flow (Karvonen, 2016). These studies have the goals of enabling efficient winter navigation and validating a fine-scale version of FMI's sea ice model (Haapala et al., 2005).

Few studies have used shipborne MR data to derive sea ice velocity fields. O'Connell (2008) explores the detectability of ice hazards (icebergs, bergy bits, and growlers) by shipboard MR, Lu et al. (2013) employ MR to estimate the ice berg distribution during a circumpolar Antarctic cruise, and Parsa (2013a, 2013b) investigate the suitability of shipborne dual-polarized MR data for ice age classification. More interestingly, in this context, Kotovirta et al. (2011) propose a prototype shipboard sensor network that includes MR for sea ice imaging and drift retrieval. The shipboard MR sea ice velocities they present, however, are limited to periods during which the ship was drifting with the ice and neglect ship motion (i.e., their velocities are relative to the ship). Similarly, Karvonen et al. (2010) and Karvonen (2016) only show shipboard MR results where ship motion has been discounted (although the former does discuss the principles of ship motion correction).

This study presents first MR sea ice velocity fields acquired from an underway research vessel over a four week period (see section 2). To retrieve sea ice drift, ship motion corrected MR sea ice images are fed into a cross-correlation-based algorithm. Results are quality controlled by ensuring similarity between neighboring drift vectors in space and time. The resulting sea ice velocity fields have a resolution of ~500 m and, under continuous processing, ~5 min (section 3). The MR sea ice velocities are validated by independent measurements from buoys that were drifting freely with the ice and from the ship during ice stations (section 4). Sea ice drift results cover the full cruise period, and several examples highlighting diverging and converging sea ice flow among other submesoscale features are presented. To investigate the physical processes driving the sea ice drift in the Beaufort Sea's fall MIZ, the MR-derived sea ice velocities are compared with simultaneous wind measurements, and put in context with measurements of the sea ice concentration and distance from the ice edge. The observed sea ice velocities reach peak values above 1 m s^{-1}, and they exhibit large spatiotemporal gradients that are only weakly correlated with the wind, suggesting that, besides atmospheric forcing, upper ocean currents play a principal role (section 5). This study concludes with a discussion (section 6) and summary of the results, including suggestions for future work (section 7).

2. Sea State Cruise and Data Overview

As part of the Sea State and Boundary Layer Physics of the Emerging Arctic Ocean program by the US Office of Naval Research, a research cruise on R/V *Sikuliaq* was conducted in the Beaufort Sea from 1 October to 10 November 2015. It involved seven wave experiments, 12 ice stations, surface flux stations, as well as ship surveys, and was complemented by both aircraft and satellite remote sensing efforts (Thomson, 2015; Thomson et al., 2018). The cruise was motivated by the dearth of in situ measurements describing the air-sea-ice system during the fall Arctic ice advance. Among other research topics, it aimed for an improved understanding of the sea state's interactions with sea ice. These are expected to gain importance as climatological trends indicate an increase in open water days, which is coupled with larger and longer waves (Stopa et al., 2016; Thomson et al., 2016).

Figure 1 shows the track of R/V *Sikuliaq* during the Sea State cruise plotted over a bathymetric map of the Chukchi and Beaufort Seas. It also shows the AMSR2-based sea ice extent (defined as the 5% ice concentration contour line) on 4 October 2015 when sea ice was first encountered and 4 November 2015 when the ship began its return to port. The ship generally stayed near the ice edge, although it would occasionally penetrate deeper into the pack ice (up to ~200 km) for ice station work. The ice edge advanced considerably during the cruise period, but also retreated sporadically in response to wind and wave events. The

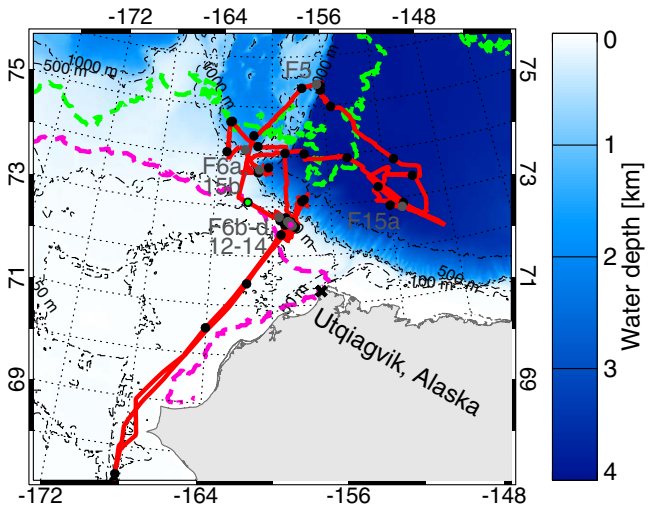

Figure 1. Map of study area in the Chukchi and Beaufort Seas. The Alaskan coastline is outlined and the black cross marks Utqiaġvik (formerly Barrow), AK. The bathymetry data were obtained from the GEBCO digital model (Weatherall et al., 2015). Contour lines are plotted along depths of 3,000, 1,000, 500, 100, and 50 m. The solid red curve marks the track of R/V *Sikuliaq*. The passage of each day is marked by a black dot. The green and magenta dashed lines mark the AMSR2-based sea ice edge (5% ice concentration contour line; data from the University of Bremen, Germany, https://seaice.uni-bremen.de/sea-ice-concentration/) for 4 October and 4 November 2015, respectively (Spreen et al., 2008). The magenta and green dots mark the corresponding ship positions. The dark gray dots mark the ship positions for several of the examples shown in this study, with the labels (F5, F6a, etc.) corresponding to the respective figure numbers.

most significant retreat occurred during a storm from 11 to 14 October, when a maximum significant wave height of ∼5 m and peak wave period of ∼10 s were measured (Collins et al., 2017; Rogers et al., 2016; Smith et al., 2018).

The MR on R/V *Sikuliaq* consists of a Sperry 9.4 GHz transceiver that is equipped with a heating element for low temperature operations (to −55°C). It has an 2.4 m horizontally polarized antenna, 50 ns minimum pulse length, 3 kHz pulse repetition frequency (short pulse mode), 25 kW peak power, and 1.25 s antenna rotation period. These radar parameters correspond to a 7.5 m range resolution and a 0.7° horizontal antenna beam width. The system employs a magnetron oscillator to generate its microwave pulses and is thus noncoherent. It is furthermore not radiometrically calibrated, as is typical for standard commercial MRs (Gommenginger et al., 2000). During the Sea State cruise, the MR was continuously operated in short pulse mode, as is required for high quality surface wave and near-surface current measurements (e.g., Lund et al., 2017). The MR is connected to Rutter's sigma S6 Ice Navigator and WaMoS, a server with a radar acquisition board and software for sea ice imaging and surface wave monitoring. The Rutter system provides the ship's primary navigation aid during in-ice operations. The analog MR signals sampled by the system include each radar pulse's logarithmically amplified backscatter intensity (video) and antenna look direction (relative to the transceiver). They are fed into an analog-to-digital converter and sampled with 12 bit resolution. The video signal has a range resolution of 3.75 m and extends up to a maximum range of 11.1 km. Here the radar data are limited to a maximum range of 4 km, since the radar return at greater ranges is usually too weak to resolve distinct sea ice features (at least in short pulse mode). The Rutter system's radar raw data were archived on a pair of dedicated Synology NAS servers (with a combined storage capacity of 64 TB) during Sea State. For this study, these data are analyzed using IDL-based software developed at the University of Miami. Figure 2a shows a picture of R/V *Sikuliaq* moored to a large multiyear floe during the first ice station on 6 October 2015. Figure 2b shows a zoom of the ship's mast; the MR used here is located above the S-band and X-band radars (used for open water navigation) at a height of 25 m above sea level.

During each of the seven wave experiments, multiple drifting Surface Wave Instrument Float with Tracking (SWIFT) and wave buoys were deployed, for the most part in ice-covered waters but also on multiyear floes and in open water near the ice edge. The SWIFTs are spar buoys equipped with a GPS receiver, anemometer, ADCP, camera, and inertial measurement unit (IMU; Thomson, 2012). The wave buoys (elsewhere referred to as "UK buoys" (Rogers et al., 2016) and "Doble/Wadhams buoys" (Wadhams & Thomson, 2015)) consist of a GPS and IMU housed in a cylindrical floater. Pictures of wave and SWIFT buoys secured on R/V *Sikuliaq* and drifting in icy seas are shown in Figures 2c–2f. This study uses the GPS positions from drifting SWIFT and wave buoys to validate the MR-derived sea ice velocities.

R/V *Sikuliaq* is equipped with a Seapath 320, an integrated multi-antenna GPS and IMU sensor providing precise heading (0.04° accuracy) and position (1 m accuracy). The Seapath measurements were sampled with 5 Hz resolution and are used for MR motion correction purposes. During ice stations, when the ship was passively drifting with larger multiyear floes to which it was moored, the Seapath positions are furthermore used as a reference measurement of sea ice drift. An atmospheric boundary layer flux package, which includes sonic anemometers at two levels, provides excellent measurements of wind velocities when the ship-relative wind is ±90° from bow-on after standard flow-distortion corrections. To avoid ship contamination of the airflow when the ship-relative wind has a component from the stern, winds from the windward unit of the two 2-D sonic anemometers located on the ship's main mast are used. These are in good agreement with the corrected bow-mast winds at 17 m above mean surface layer for bow-on winds (Persson et al., 2018). These composite wind velocities are used to investigate the atmospheric forcing effect on the

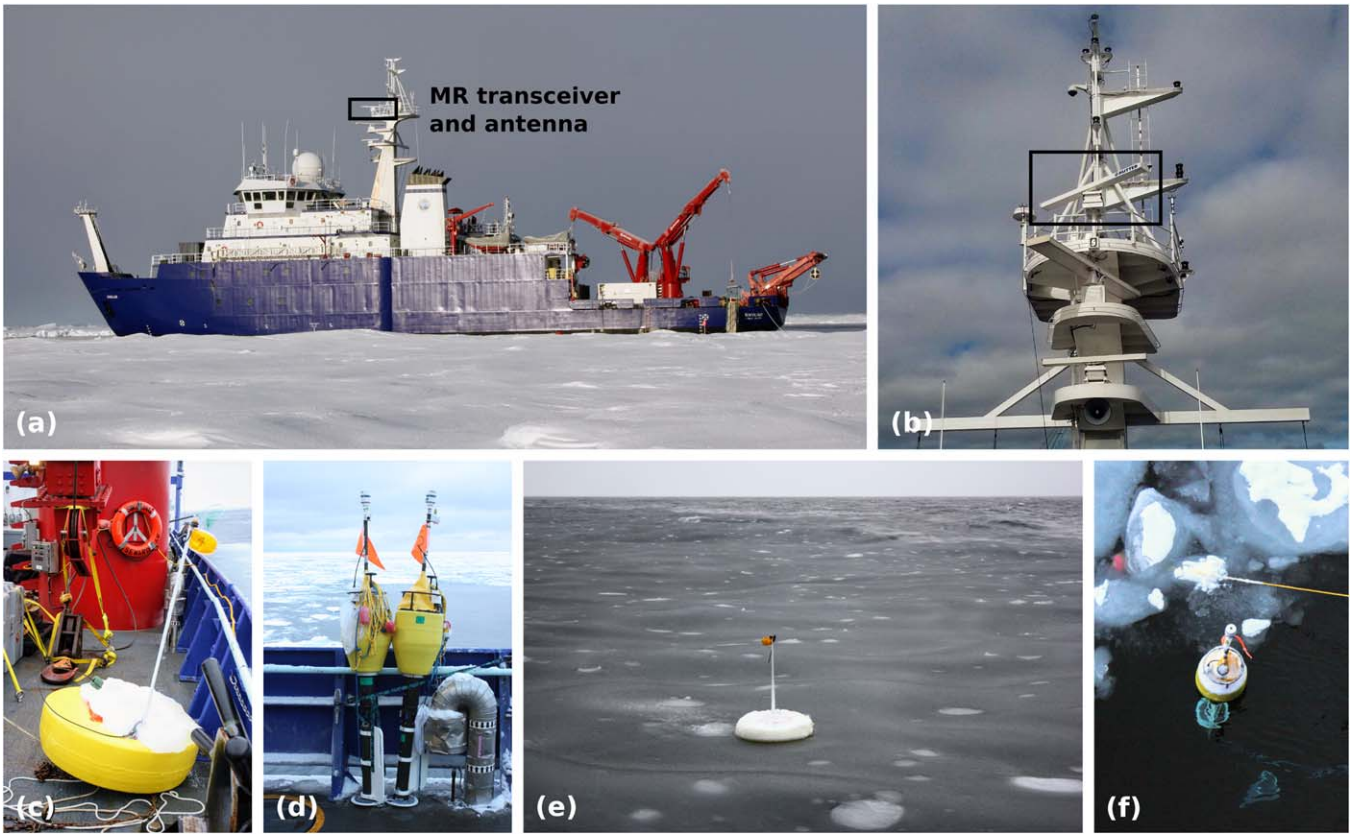

Figure 2. (a) Photos of R/V *Sikuliaq* during an ice station on 6 October 2015 and (b) a close-up of the ship's mast. The MR transceiver and antenna are framed by a black rectangle. (c) Photos of a postdeployment wave buoy on the deck of the ship and (e) in waters dominated by pancake and frazil ice. (d) Photos of a pair of predeployment SWIFT buoys and (f) a SWIFT buoy drifting alongside snow-covered first-year ice during recovery.

MR-derived sea ice drift. The local ice concentrations used in this study represent a combination of daily AMSR2 satellite estimates at 3.125 km resolution (provided by the University of Hamburg, Germany, via ftp://ftp-projects.cen.uni-hamburg.de/seaice/AMSR2) with shipboard visual and radiometric estimates. Lastly, AMSR2 data were consulted to determine the ship's distance from the ice edge (Beitsch et al., 2014). For more details on these wind and ice data, see Persson et al. (2018).

3. Sea Ice Drift Retrieval Methodology

3.1. Radar Data Preprocessing

Before sea ice drift retrieval, the raw MR backscatter intensities must undergo several preprocessing steps. This study computes sea ice drift over analysis periods of ∼5 min. The preprocessing steps described in the following are performed for each analysis period.

If other X-band radars are operating on the same or nearby vessels, the measured radar backscatter intensity exhibits frequent interference spikes (typically, multiple spikes per antenna rotation). These spikes are characterized by elevated radar returns that are limited to few (on the order of 10) range bins within a single pulse. Here a convolution kernel that enhances the radar interference spikes is used to locate them. They are replaced by (azimuthally) neighboring valid data using linear interpolation.

According to the radar equation for distributed targets like the sea surface, the radar backscatter intensity decay with range is cubic (e.g., Haykin et al., 1994). To increase the radar video signal's dynamic range, commercial radars are equipped with logarithmic amplifiers. The radar manufacturers generally do not disclose the exact form of the amplification function used, but they are known to depart from the pure logarithmic form (Gommenginger et al., 2000). The MR data at hand exhibit a pronounced decay in backscatter intensity from near to far range. For the sea ice drift retrieval, it is important that the radar images have means and

standard deviations that are range independent (as will become evident in the next subsection). Lacking an analytical expression to correct for the range dependency, this study uses an empirical approach. From ~5 min worth of despiked backscatter intensities, the mean and standard deviation over all azimuths are determined as functions of range. The resulting ramp-like curves are smoothed using a box car average filter. To remove the range dependency in the MR data, for each range coordinate, the corresponding mean backscatter intensity is subtracted, and the result is divided by the corresponding standard deviation. Here the resulting backscatter intensities are referred to as normalized. The backscatter intensity's upwind peak (e.g., Lund et al., 2012) is negligible in ice covered seas, and hence it is not accounted for.

For MR-based near-surface current retrieval, as with shipboard ADCPs, it is important that an accurate heading device (with an accuracy of 0.1° or better) be used and that any offsets between the radar image and ship heading (or, in the ADCP example, between transducer and ship heading) be removed. Heading errors will lead to erroneous cross-track currents, with the error being proportional to the product of the ship speed and the sine of the offset angle (Lund et al., 2015). The same rules apply to shipboard MR sea ice drift retrieval. For example, with R/V *Sikuliaq* transiting at 11 kn, a 1° bias in the MR image heading will result in a 0.1 m s^{-1} error in the sea ice velocity's cross-track component. Here the ship's highly accurate Seapath compass is used, and a constant −1.32° MR image heading offset, identified following the "calibration" procedure outlined in McCann and Bell (2018), has been corrected for.

With the MR backscatter intensity measurements despiked and normalized, and image heading offsets corrected for, the data are ready for ship motion correction or, in other words, georeferencing. Here only the horizontal ship motion, measured by the Seapath GPS, is accounted for, i.e., the ship's heave, pitch, and roll are neglected (mapping errors associated with these motions are generally smaller than the MR range resolution and will average out). Furthermore, for simplicity, Earth is assumed flat, which is reasonable given the MR's short maximum range of 4 km. The georeferencing is done on a pulse-by-pulse basis, which requires that the antenna look direction (relative to north) and radar transceiver position are determined for every MR pulse. This is accomplished by linearly interpolating the 5 Hz Seapath measurements to match the MR's 3 kHz pulse repetition frequency. The radar pulses associated with each complete antenna rotation are mapped onto a Cartesian grid using bilinear interpolation. The Cartesian grid has 7.5 m resolution (the MR's range resolution) along both the *x* and *y* axes, which have west-east and south-north orientations, respectively. Pixels with data points from multiple pulses are averaged according to each data point's interpolation weight. Image pixels where the ship was in the very near range include measurements from ~30 pulses or more. The pulse-by-pulse georeferencing (as opposed to a nearest neighbor approach) therefore greatly improves a MR target's signal-to-noise ratio. The result of the georeferencing is a three dimensional (*x*, *y*, *t*) array of ship motion corrected backscatter intensity images, which forms the basis of the sea ice drift retrieval described in the next subsection.

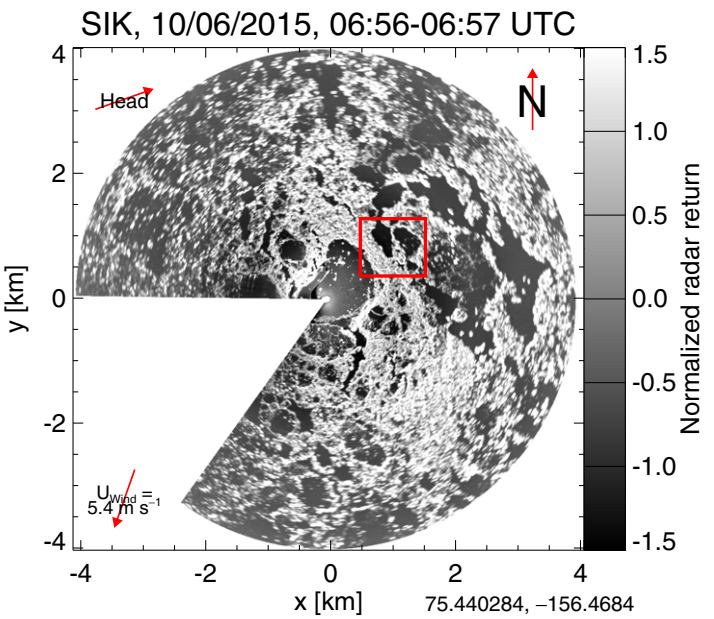

Figure 3. Example of a MR sea ice image collected from R/V *Sikuliaq* on 6 October 2015, from 06:56 to 06:57 UTC. The normalized radar return is shown on a gray scale (weak return is shown in black, strong return in white). The red square marks one sea ice drift analysis window. The corresponding wind direction, ship heading, and the image's geographic orientation are given by the arrows in the corners of the reference frame. The position of the coordinate frame's origin (latitude and longitude in decimal degrees) is printed in the bottom right.

3.2. Maximum Cross Correlation

Figure 3 gives an example of a 1 min averaged MR sea ice image acquired from R/V *Sikuliaq* on 6 October 2015, 06:56 UTC. The image includes a 55° sector toward the stern that is shadowed by the main mast. At the image acquisition time, the ship was traveling east-northeast into the pack ice with a 5 m s^{-1} wind from north-northeast. The ice concentration at the ship position (based on AMSR2, visual, and radiometric estimates) was 99% and the AMSR2-based distance from the ice edge was −144 km. The MR image confirms a full ice cover with alternating patches of first-year and multiyear ice, which offer well defined features for sea ice drift retrieval.

Cross correlation between two normalized images that are separated in time (here referred to as reference and search images) is a

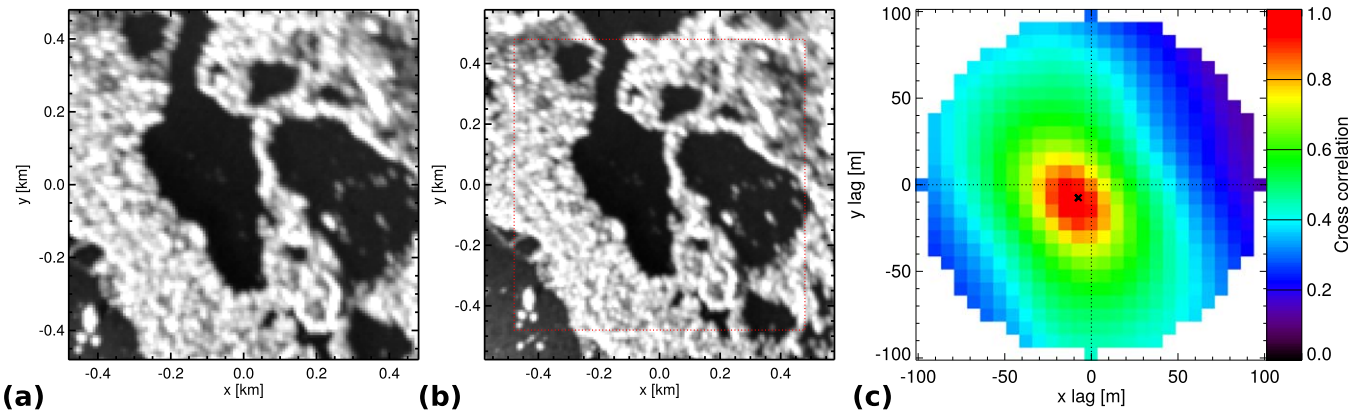

Figure 4. (a) Reference image within the sea ice drift analysis window marked in Figure 3 and (b) corresponding search image acquired 75 s later. The larger search image is centered around the reference image location, which is marked by a red dashed square. Both images use the same gray scale as in Figure 3. (c) Cross correlation of reference and search image on a color scale from black (no correlation, $r = 0$) to red (perfect correlation, $r = 1$). The MCC is marked by a black cross.

commonly used technique for automated sea ice drift retrieval (e.g., Emery et al., 1986; Fily & Rothrock, 1987; Karvonen et al., 2010). Figure 4 illustrates the technique for one analysis window, covering the same period as Figure 3. The reference image in Figure 4a has an edge length of 960 m (128 pixels), its location is outlined by the red square in Figure 3. The choice of image size is a compromise between the desire for high spatial resolution on the one hand and the necessity to have sufficient sea ice signal under a broad range of conditions on the other hand. The search image in Figure 4b was acquired 75 s later and has an edge length of 1,155 m (154 pixels), it is centered around the reference image's location. The size of the search image is determined by the maximum expected sea ice speed, which here is set to 1.25 m s^{-1}, and the separation time (75 s). Both reference and search images represent 1 min averages, i.e., they are based on 48 consecutive scans (given a 1.25 s antenna rotation period). Compared with a single scan, the averaging greatly enhances the sea ice signatures (it also serves to obscure surface wave signatures, see section 3.4). Karvonen et al. (2010) use a median filter to a similar effect.

In this study, the cross correlation is determined by computing the Pearson product-moment correlation coefficient between reference and search image for all possible lags (within the 1.25 m s^{-1} limit). The resulting cross-correlation matrix consists of 27 by 27 pixels where the center pixel corresponds to zero lag. Alternatively, fast Fourier transforms (FFTs) could be employed to compute the cross correlation more efficiently (e.g., Kwok et al., 1990). Figure 4c shows the cross correlation between reference and search image, which has a maximum of 0.98 and a minimum of 0.13. The correlation coefficient serves as a measure of the similarity between the image pairs. Here the lag associated with the maximum cross correlation (MCC) is interpreted as the relative location of a matching sea ice feature (more on this in the next subsection). The MCC's x and y lags divided by the separation time provide a first rough estimate of the sea ice velocity, namely a speed of 0.14 m s^{-1} and a direction of 225°. The 75 s separation time between images implies that an x or y lag of one pixel corresponds to 0.1 m s^{-1}, which is too coarse a resolution for our purposes. To achieve subpixel precision in both x and y directions, second order polynomials are fitted to the peak and its two direct neighbors using the least squares method. A precise sea ice velocity is obtained from the fit functions' peak locations. In this example, the resulting sea ice speed and direction are 0.19 m s^{-1} and 226°. To reduce the processing time and avoid false matches, only lags with corresponding speeds $\leq$1.25 m s^{-1} are considered.

The sea ice drift analysis is performed over a set of analysis windows that uniformly cover the radar field of view (FOV), with a 50% overlap between neighboring windows. Figure 5 gives the sea ice velocity field for the same analysis period as in Figures 3 and 4. The observed sea ice vectors appear spatially coherent. For a total of 156 sea ice drift vectors, the speed ranges between 0.14 and 0.20 m s^{-1} with a mean of 0.17 m s^{-1}, and the direction ranges between 208° and 243° with a 226° mean. The mean values indicate a 14° deflection to the right of the wind and a 3% speed factor.

3.3. Similarity-Based Quality Control

The cross-correlation-based technique described in the previous subsection will yield drift estimates for the entire radar FOV, even for analysis windows that do not have distinct sea ice features. Here false sea ice

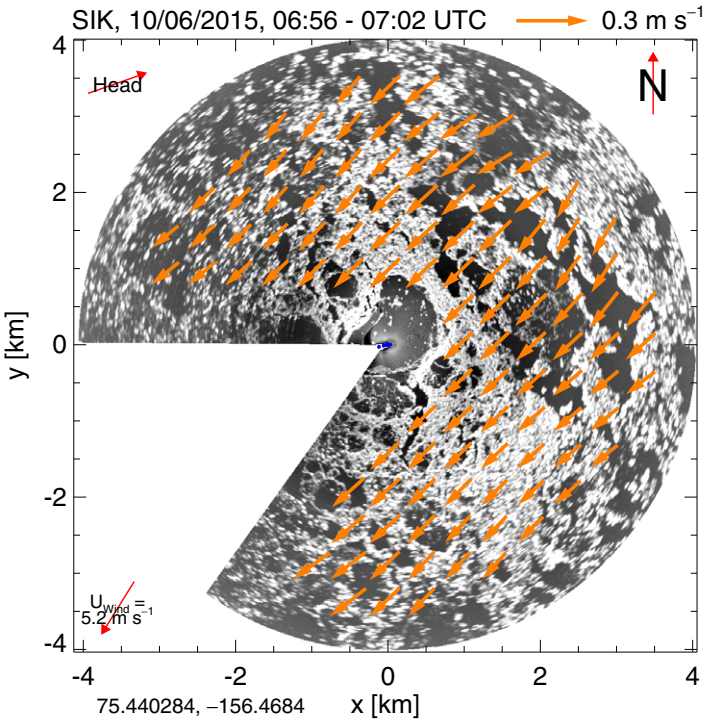

Figure 5. MR sea ice image (same as in Figure 3) and velocity field from R/V *Sikuliaq* on 6 October 2015, from 06:56 to 07:02 UTC. The orange arrows indicate the local sea ice speed (see legend in the title, top right) and direction. The blue dots in the center indicate the ship track during the analysis period. The gray scale is the same as in Figure 3.

velocities are identified by evaluating the similarity between spatially and temporally neighboring drift estimates. In order to obtain a first set of temporally neighboring sea ice velocity pairs, the drift retrieval is repeated with the search (second) image from the prior analysis serving as reference (first) image and the 1 min averaged MR image from 75 s later as the new reference image. A second set of sea ice velocity pairs is obtained by repeating this process but using an extended 3 min averaging period (hence, the need for a ∼5 min analysis period). More on the extended averaging period in the following subsection. The result consists of four "temporally" neighboring sea ice velocities per analysis window. The temporal quality control uses their marginal median as reference. The difference vectors between all four sea ice velocity estimates and their reference must have magnitudes < 0.1 m s^{-1} for the given analysis window to pass. The sea ice velocities reported here are averages over each temporal set. To evaluate the spatial similarity, all directly neighboring drift estimates are considered, including the diagonally adjacent ones (maximum eight neighbors). The difference vector between each sea ice velocity and the marginal median of its neighbors must have <0.2 m s^{-1} magnitude. Based on visual inspection of all the quality-controlled sea ice drift fields and the corresponding sea ice images, this method eliminates nearly all false sea ice velocities and is thus adequate for this data set.

Figure 6 gives examples of sea ice velocity fields where false vectors were removed by the quality control. In addition to the MR-derived vectors, the figure shows all corresponding SWIFT and wave buoy drift velocities and positions. Figure 6a includes patches of smooth first-year ice that are lacking distinctive features for sea ice drift retrieval (top left of figure). The quality control successfully eliminated the corresponding sea ice drift measurements. The remaining vectors indicate a largely uniform sea ice drift field with a mean speed and direction of 0.37 m s^{-1} and 347°. Figures 6b and 6c show the ice edge with large patches of open water (bottom left of both figures). Velocities associated with open water were successfully eliminated by the quality control. The sea ice drift exhibits a large degree of spatial variability, especially in Figure 6c where drift speeds range from 0.00 to 0.15 m s^{-1} covering a broad spectrum of directions. Lastly, Figure 6d gives another example of a uniform sea ice drift field with speeds ranging from 0.70 to 0.86 m s^{-1} and directions from 313° to 324°. Several vectors failed quality control for lack of well-defined sea ice features (bottom left of figure). The MR sea ice and buoy drift vectors are in excellent qualitative agreement. In particular, the buoy vectors support the MR-based observation that there is an elevated spatial variability in the sea ice drift near the ice edge. Furthermore, it is noteworthy that the observed sea ice drift vectors are generally poorly correlated with the wind. The exception is Figure 6d, where the mean sea ice drift is 18° to the right of the wind with a 7% speed factor.

3.4. Motion Estimation During Energetic Wave Event

One of the goals of the Sea State cruise was to study wave-ice interactions. During the 11–14 October wave event, with significant wave heights reaching ∼5 m, the surface wave signatures were the most prominent signal in the MR backscatter intensity images. Figure 7 shows MR measurements from 13 October 2015, 06:00 UTC, covering a square area with ∼3 km edge length. The sea ice at the time was characterized by pancake and frazil ice with spatially varying concentrations (as in Figure 2e). The wind speed was 13.5 m s^{-1} from 117°, and the MR-derived sea ice drift has a mean speed of 0.34 m s^{-1} and direction of 296° ("going to"). The backscatter data in Figure 7a are based on a single MR scan, i.e., no temporal averaging. The surface waves are clearly visible as quasi-periodic bands of enhanced and reduced backscatter. They have been observed to propagate at close to their respective linear phase speeds (Cheng et al., 2017). An extended averaging period is necessary to completely eliminate the surface wave signal. Thus, during this wave event, only sea ice drift estimates that are based on a 3 min averaging period are considered (see

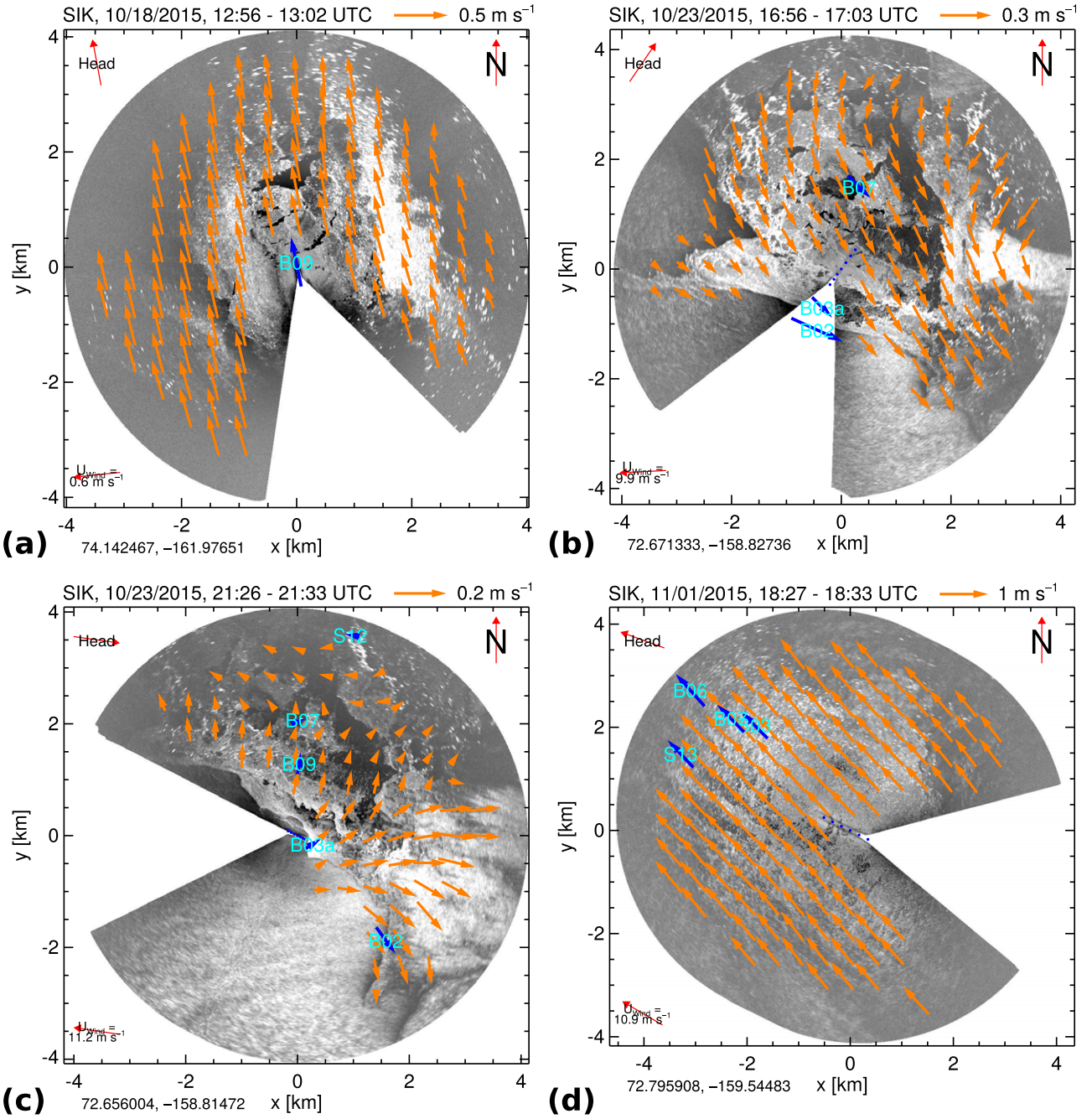

Figure 6. Examples of MR sea ice velocity fields acquired from R/V *Sikuliaq* on (a) 18 October 2015, 13:00 UTC, (b) 23 October 2015, 17:00 UTC, (c) 23 October 2015, 21:30 UTC, and (d) 1 November 2015, 18:30 UTC. The MR drift vectors are shown in orange, with each figure having its own reference vector in the title. Where available, buoy drift measurements are plotted on top in blue. The reference vectors' labels give the buoy number and type (S, SWIFT; B, wave buoy).

previous subsection). Figure 7b shows the corresponding 3 min averaged backscatter intensity. The averaging enhances the sea ice features considerably, such that the wave signal is no longer visible. To compensate for the reduced number of sea ice velocity estimates per analysis window, a MCC threshold of 0.7 is used to identify and remove outliers. (This makes sense since the MCC is a measure of similarity between image pairs.) In general, the similarity-based quality control described in the previous subsection is good enough for separating signal from noise.

However, the extended averaging presents a problem of its own. For example, sea ice drifting at 1 m s^{-1} along the *x* or *y* direction will have moved across 24 pixels over the averaging period. The averaging will

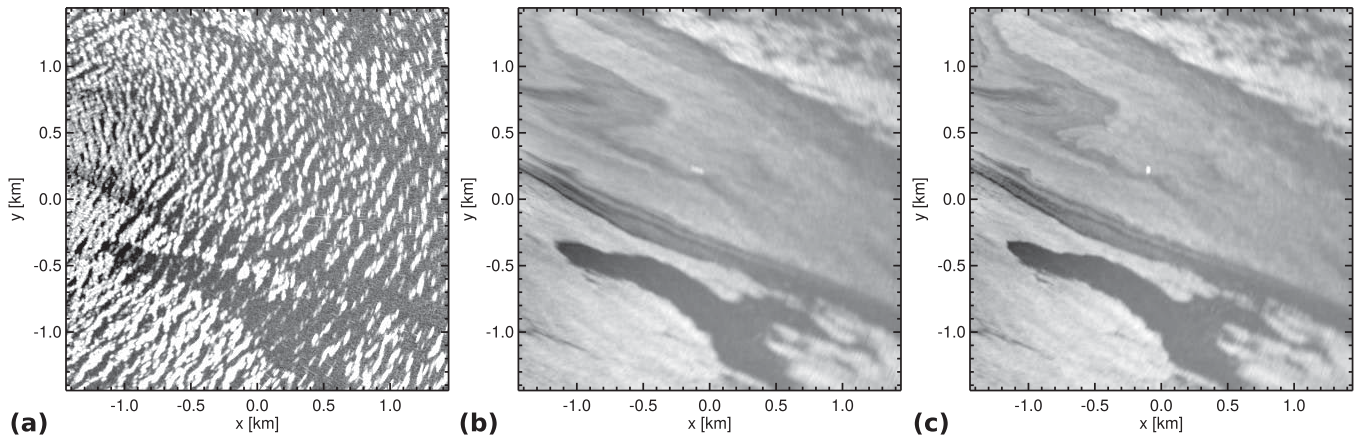

Figure 7. MR sea ice image from 13 October 2015, 06:00 UTC, (a) without temporal averaging, (b) with 3 min averaging, and (c) with 3 min averaging as well as sea ice drift correction. All figures use the same gray scale as in Figure 3.

therefore blur the sea ice signal. This issue is addressed by making first guess sea ice velocity estimates for each analysis window. These estimates are based on pairs of (potentially) blurred sea ice images. The resulting velocities are then used to correct for the sea ice drift before averaging once again and repeating the sea ice drift analysis with the thus sharpened images. (This additional processing step is especially important here due to the relatively faint sea ice signal.) Figure 7c shows the 3 min averaged MR image post sea ice drift correction. While the figure looks similar to Figure 7b, the sea ice features are better defined. For example, note the MR backscatter intensity peak at (–100, 200 m), stemming from a drifting wave buoy. The buoy is next to impossible to detect in the single scan image (Figure 7a), and in the original averaged image its drift produces a linear feature with normalized backscatter intensities that are comparable with those of neighboring sea ice patches (Figure 7b). But in the sea ice drift corrected and averaged image, the buoy stands out as a bright point-like feature. (As a side note, the MR sea ice images shown in Figures 5 and 6 represent sea ice drift corrected radar images that were averaged over the entire ∼5 min analysis period. An extended 3–5 min averaging period provides an easy means of assessing the effectiveness of the sea ice drift retrieval. The presence of sharp sea ice features indicates accurate MR drift velocities. Here the image sharpness is evaluated visually, but a numerical evaluation, e.g., based on local gradients, is certainly possible.) A comparison with photographs taken from R/V *Sikuliaq* around the time of measurement suggests that the frazil ice present here reduces the MR backscatter intensity compared with the open water. This can be explained by the frazil ice's smooth surface and its dampening of the short scale Bragg waves. In contrast, the sea ice within the images shown in Figures 5 and 6 enhances the backscatter intensity.

4. Validation of Sea Ice Velocities

The validation of the MR sea ice velocities is based on independent drift measurements from SWIFT and wave buoys as well as R/V *Sikuliaq* during ice stations. The MR and reference sea ice velocity measurements are spatially and temporally collocated. In case a reference measurement lies inside a MR velocity field, the four surrounding MR velocities are interpolated bilinearly to exactly match the reference position. Else, all MR measurements within a distance of 679 m ($\sqrt{2}\times$480 m, where 480 m is the vertical and horizontal distance between MR estimates) from the reference measurement are averaged and retained for comparison.

Figure 8 shows scatterplots of the MR and reference sea ice velocity measurements for *u* and *v* (corresponding to the west-east and south-north directions). While the MR velocities correlate well with all reference sensors, the agreement is best for the comparison with R/V *Sikuliaq* followed by that with SWIFT buoys. The corresponding comparison statistics are given in Table 1. The correlation coefficients r^2 are generally high (ranging from 0.94 to 1.00) and biases low (from -0.65 to 0.15 cm s^{-1}). As evident from the scatterplots, the root-mean-square (RMS) errors for the MR versus R/V *Sikuliaq* comparison are lowest at $<$1 cm s^{-1} for both *u* and *v* (with median percent differences of $<$10%). The MR-SWIFT RMS values are $<$3 cm s^{-1} and the MR versus wave buoy values are $<$6 and $<$4 cm s^{-1}, respectively. (The corresponding median percent

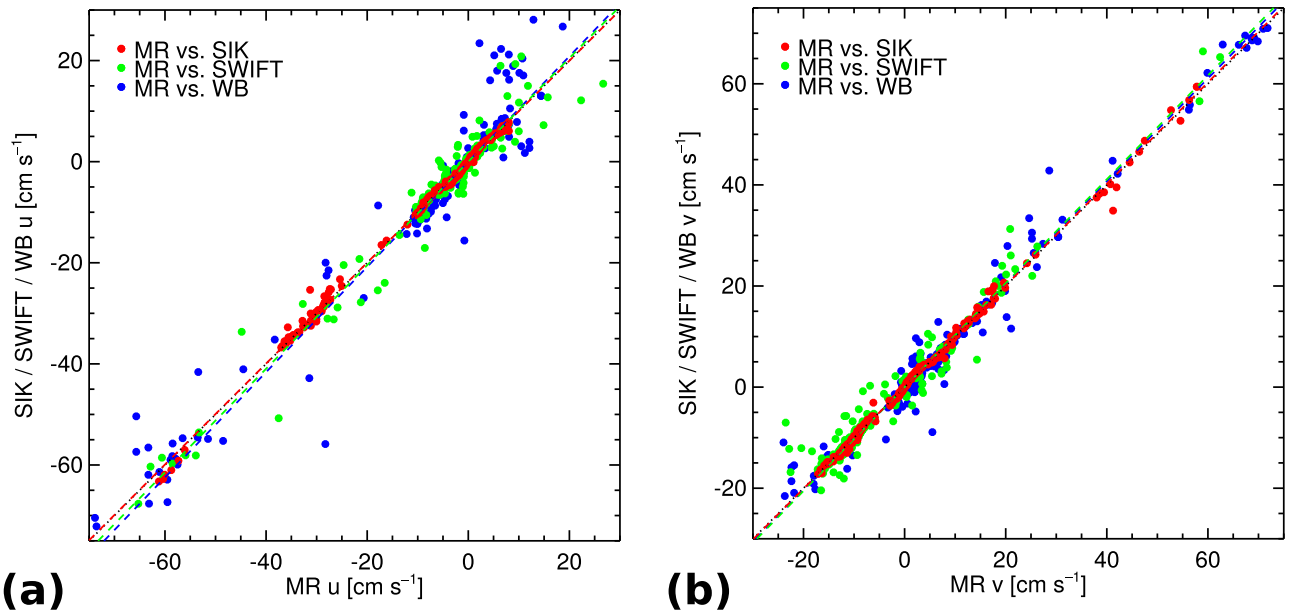

Figure 8. Scatterplots of MR versus SWIFT (green dots), wave buoy (blue), and R/V *Sikuliaq* (red) measurements of (a) the *u* (west-east) and (b) *v* (south-north) components of the sea ice drift. The dashed lines give the corresponding best fit lines.

differences range between 8 and 26%.) Statistical comparisons of the same data in terms of sea ice drift speed and direction can be found in the supporting information as Table S1.

A movie showing all MR sea ice velocity fields (yellow vectors) is included as supporting information S2. The MR vectors are plotted over the corresponding normalized MR backscatter intensity images (black = weak return, white = strong return). The movie furthermore includes SWIFT and wave buoy drift vectors (plotted in red) where available. The movie's frames update every 30 min and range from 4 October to 4 November 2015 (1,417 frames total). For a small percentage of movie frames, no sea ice velocity information is available despite distinct sea ice features (e.g., approximately every other frame between 28 October 2015, 12:30 UTC and 29 October 2015, 12:30 UTC). This is due to MR data dropouts, which precluded a reliable sea ice drift retrieval. In these cases, the sea ice images may appear blurred for lack of a sea ice drift correction prior to averaging (see section 3.4).

5. Sea Ice Drift in the Beaufort Sea's Fall MIZ

5.1. The Physical Controls

The ice momentum equation combined with drag formulations of the atmospheric and oceanic stress (e.g., Schweiger & Zhang, 2015) show that acceleration of sea ice (changes in the ice velocity vector) is directly a function of the square of the wind speed, the square of ocean current velocity, the Coriolis force, internal

Table 1
MR-SIK, MR-SWIFT, and MR-WB Comparison Statistics for Sea Ice Drift's *u* and *v* Components (SIK = R/V *Sikuliaq*, WB = Wave Buoy)

	MR-SIK		MR-SWIFT		MR-WB	
	u	*v*	*u*	*v*	*u*	*v*
N	255	255	218	218	158	158
r	1.00	1.00	0.97	0.98	0.97	0.99
r^2	1.00	1.00	0.95	0.95	0.94	0.97
Bias (cm s^{-1})	0.02	0.02	0.15	−0.42	−0.65	−0.02
RMS (cm s^{-1})	0.75	0.77	2.96	2.75	5.65	3.33
σ_{xy} (cm s^{-1})	0.75	0.77	2.96	2.72	5.61	3.33

ice stress, and the ocean surface slope. The internal ice stress is a function of several ice parameters, including ice concentration. The various forcing terms have different magnitudes and directions, with some terms acting at sharp angles to others or directly opposing them. Early researchers noted that the ice drift is primarily forced by the wind stress, so empirical relationships between the wind and the ice drift vectors have been suggested. Based on 3 years of data from his seminal transpolar drift in 1893–1896, Nansen (1902) found that the ice drift speed was 1.8% of the wind speed (surface wind factor), with an ice drift deviation angle (ΔDir = ice drift "from" direction minus wind direction) of +28° (to the right of the wind). These values are consistent with more recent estimates (Martinson & Wamser, 1990; Grumbine, 1998; Skiles, 1968), with Leppäranta (2011) concluding that typical values for the Arctic wind factor and deviation angle are 2% and 30° (to the right of the wind), respectively. For the central Arctic Ocean, Thorndike and Colony (1982) found that more than 70% of the sea ice velocity variance (on time scales from days to months) can be explained by geostrophic wind, and such high correlations between the wind and ice drift are typical (e.g., Persson, 2011; Schweiger & Zhang, 2015). In the MIZ, however, large spatiotemporal gradients in mixed layer temperature, salinity, and surface wind drag result in strong submesoscale currents, which in turn have a major impact on sea ice dynamics (Manucharyan & Thompson, 2017; McPhee et al., 1987; Timmermans et al., 2012). Sea ice generally drifts freely in the MIZ and hence has higher mobility compared with the central Arctic pack ice (McPhee, 1980). Gimbert et al. (2012) showed that inertial oscillations are strong in loose ice cover, but become undetectable in compact ice cover where they are damped by internal stresses. Furthermore, satellite observations indicate that mesoscale eddies and meanders are important features near the ice edge (Johannessen et al., 1987a, 1987b).

To investigate the physical controls of sea ice drift in the Beaufort Sea's fall MIZ, the sea ice speed and direction observed by the MR on the R/V *Sikuliaq* were compared with the Sea State observed and quality-controlled wind vectors. The sea ice drift values were computed following the methodology described in section 3. They represent spatial averages over the sea ice drift vectors that passed quality control, and were updated in 30 min intervals. The data begin with the ship's first encounter of sea ice on 4 October 2015, and end on its return to port on 4 November 2015. The corresponding 10 min wind speed and direction at 17 m height above the water surface represent an optimization of the various shipboard anemometer measurements, while ice concentrations represent a combination of daily AMSR2 satellite estimates with onboard, along-track visual and radiometric estimates (see section 2 for further details). A time series comparison for the entire cruise is shown in supporting information Figure S3, while scatterplot comparisons are shown in Figure 9. The MR sea ice drift is highly variable with speeds ranging from 0.00 to 1.02 m s^{-1}, a mean speed of 0.26 m s^{-1}, and a standard deviation of 0.19 m s^{-1}. The equivalent wind speed values are 0.3–16.7, 6.4, and 4.2 m s^{-1}, respectively. Sea ice and wind directions cover a broad range of values with respective means of 102° and 60° (both "from"). The sea ice concentrations along the track of R/V *Sikuliaq* have a mean value of 73%. Based solely on AMSR2, the mean distance from the ice edge was −58 km with a −198 km minimum.

Figure 9 shows that the relationship between the onboard winds and the MR ice drift vectors in the vicinity of the ship is complicated and not as simple as the wind-ice drift relationships suggested by previous studies. The ice drift speeds in Figure 9a have been multiplied by 20, so the 1:1 line represents an ice drift of 5% of the wind speed. Many of the ice drift speeds are above this value and many are below, with a relatively poor correlation of $r = 0.58$ ($r^2 = 0.34$). The bin-averaged values (black cross) suggest a percentage that decreases with increasing wind speed from above 5% at low winds to about 3.5% at 11 m s^{-1}, though again the scatter is very large (the overall mean is 5.0%). In terms of sea ice and wind direction, the mean directional difference length (correlation coefficient for directional data, defined as the length of the vector mean of the set of unit vectors whose directions are set to the angle differences between the two series; 1 indicates perfect correlation) R is 0.88. The drift angle average is to the right of the wind direction by +18° (dotted line in Figure 9b), but this mean is composed of two distinct drift regimes. The mean drift angle is +23° to the right of the wind for the first wind sector, which includes all wind directions except the SSE-W sector (160°–280°). However, when the wind is from the SSE-W sector, the ice drift averaged about −42° to the left of the wind; that is, on the opposite side of the wind vector than expected from wind drift alone. The ice drift velocity for this wind sector averaged slightly higher than 5% of the wind speed (see blue points and line in Figure 9a), though these drift directions to the left of the wind were predominantly associated with wind speeds under 10 m s^{-1}. Note that a frequent number of drift vectors had an absolute direction difference >90°; that is, many points had a drift component opposing the wind.

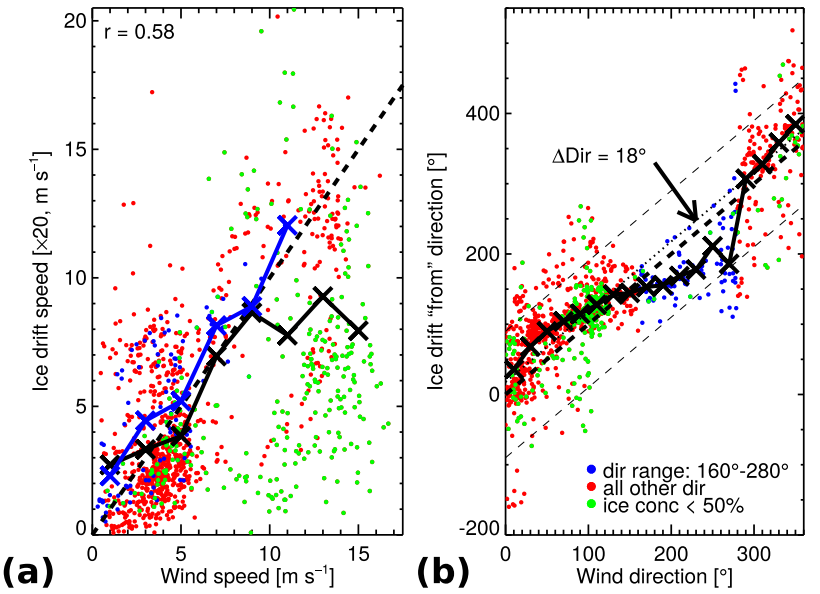

Figure 9. Scatterplots of (a) ice drift speed as a function of wind speed and (b) ice drift direction as a function of wind direction. Wind speeds are the best estimate 10 min, 17 m winds from the R/V *Sikuliaq* while the ice drift values are from the MR cross-correlation technique. Blue points correspond to wind directions between 160° and 280°, red points correspond to all other wind directions, while green points are those with an ice concentration <50%. In Figure 9a, the correlation coefficient *r* is computed using all points. The solid lines connect bin-averaged values, indicated by cross (black = all points, blue = wind directions from 160° to 280°). The ice drift speed has been multiplied by 20. In Figure 6b, the thin dashed lines are 90° from the 1:1 line (heavier dashed line). ΔDir (=ice drift direction minus wind direction) is the turning angle. The dotted line marks the mean ΔDir.

Stratification of the data by ice concentration shows that many of the slower drift speeds occur for low ice concentrations (e.g., green points in Figure 9). By examining the wind-ice drift correlation in specific ice concentration categories, it can be seen that the correlation between the wind speed and the drift speed is especially poor for ice concentrations <50%, while it becomes quite good and close to 5% of the wind speed for ice concentrations >85% (Figure 10). The drift angle relationship to the wind direction seen in Figure 9b does not vary with ice concentration (not shown).

The observed 3.5%–5% drift velocity relative to the wind speed is significantly higher than the 0.8%–3% values suggested by previous studies, and this increase is consistent with the satellite observations of increasing drift velocities in the central Arctic over the last few decades (Kwok et al., 2013). However, the observed

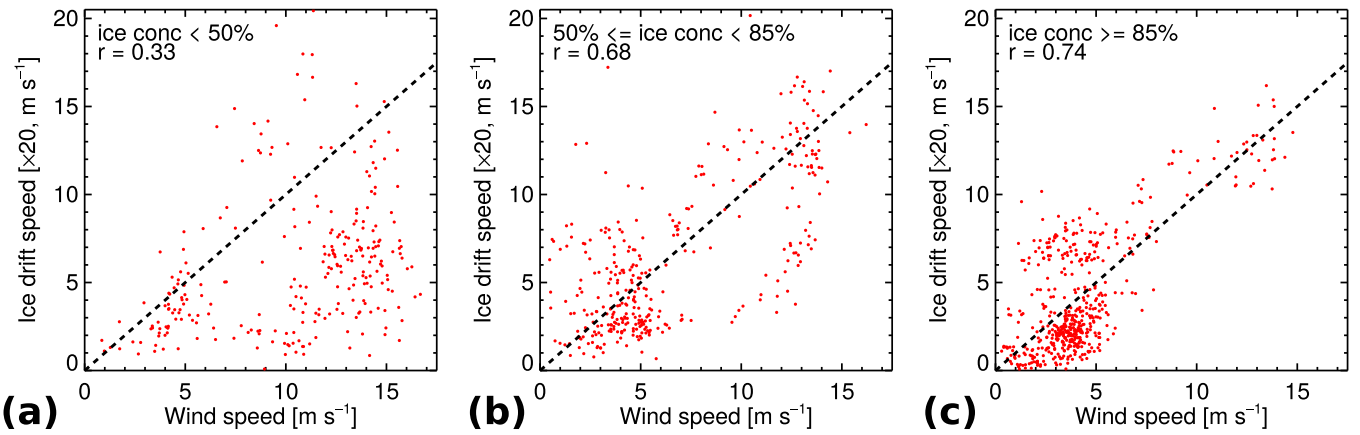

Figure 10. Scatterplots of ice drift speed as a function of wind speed for ice concentrations (a) <50%, (b) ≥ 50% and <85%, and (c) ≥ 85%. The ice drift speed has been multiplied by 20. The correlation coefficient *r* is shown for each figure.

higher wind factor for higher ice concentration contradicts the suggested cause of the basin-wide increase in ice drift speeds, which is a decrease of ice concentration.

Many low wind factors occurred on 12–13 October during a strong wind and wave event in the presence of melting ice (see Smith et al., 2018). The ice concentration averaged 33% for these 2 days but varied between 0% and 78%. The wind factor averaged 2.0% (0.5%–3.8%) and the turning angle averaged +14°, but varied between −23° and +83°. Another example of low wind factors occurred late on 24 October, when the ice concentration was 7% (consisting of streamers of pancake ice), the wind was 9.4 m s^{-1} from 88°, and the ice drift was 0.11 m s^{-1} from 355°. This is a low wind drift factor of 1.2% and a turning angle of −93° (to the left of the wind). The MR ice drift during both time periods is in good agreement with the buoy drift velocities, and is hence believed to be correct. As much of the ice on 12–13 October consisted of thin, melting pancake ice or frazil ice with little freeboard and small-scale thickness variability, we hypothesize that the ice surface roughness was likely low during this period reducing wind drag on the ice compared to periods with thicker ice and distinct freeboard and surface roughness. This is consistent with many MR images during this period which showed higher backscatter from open water areas and lower backscatter from ice-covered areas. For the 24 October case, the wind-induced ice drift is possibly counterbalanced by the influence of strong submesoscale currents near the ice edge. Hence, for both cases, there is a suggested increased importance of ocean current stress, and possibly other forcing terms, compared to the wind stress, either by reduction of the wind stress on the ice by a reduction of the ice surface roughness because of ice type or an increase in the local ocean current and ocean stress.

The reason for an ice drift turning angle with an opposite sign compared to that expected for wind directions from the SSE-W is not clear. Further examination of the negative ΔDir shows that many, but not all, of them were collected when the R/V *Sikuliaq* was near the shelf break of the Chukchi Sea. This is an area where strong ocean currents and eddies, especially from the southeast, may occur (e.g., D'Asaro, 1988) which would oppose the drift resulting from a positive turning angle by winds from this sector. However, the relatively high wind factors associated with these anomalous turning angles (blue points in Figure 9a) are inconsistent with this mechanism. Time series from 3 days when the ship was near the shelf break (Figure 11) and ice concentrations were >50% show that a strong inertial oscillation, as suggested by the 12.5 h period in the speed and direction data, existed in both the wind and ice drift, but that these oscillations were out-of-phase with each other. As a result, many negative turning angles occurred as well as some large positive ones. The large and varying drift velocities during a time of low wind speeds on 16–17 October, year days (YDs) 289–290, could have been due to ocean eddies evident in satellite SAR imagery of the sea ice structure during this time (see supporting information Figure S4; a 1 h period from 17 October where the ship encountered a small-scale eddy or meander will be discussed further in section 5.3). Additional periods with out-of-phase inertial oscillations occurred on 6–8 October (YDs 279–281) and 19–21 October (YDs 292.5–294), as shown in supporting information Figure S5. These periods again suggest that other forcing terms in the ice momentum equation may at times dominate over the wind stress term, increasing the scatter in the wind-ice drift correlations.

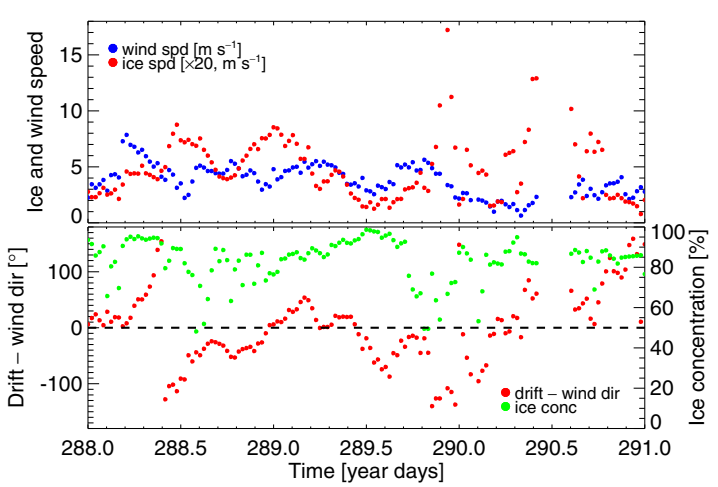

Figure 11. Time series of (top) R/V *Sikuliaq* 17 m wind speed (blue) and marine radar ice drift speed multiplied by 20 (red) and (bottom) ice drift turning angle (red) and ice concentration (green) for 15–17 October, 2015 (YDs 288–290). The dashed line in the bottom figure represents a 0° turning angle and 50% ice concentration, respectively. The short gap around YD 290.5 is due to a MR data acquisition failure.

5.2. Examples of Converging and Diverging Drift

Diverging sea ice may result in the opening of leads. During the Arctic winter, leads control the air-sea exchange of heat and moisture (Padman & Kottmeier, 2000). They also affect the sea ice mass budget and brine production, as ice grows faster in open water or thin ice than thicker ice (Holloway & Proshutinsky, 2007). Converging sea ice may lead to ice thickening through rafting or ridging (Thorndike et al., 1975). According to a modeling study by Heil and Hibler (2002), sea ice deformation due to subdaily motions increases winter ice mass by ∼20%. Measuring sea ice velocity gradients at short time scales is difficult as it requires an array of position measurements (Hutchings & Hibler, 2008) or the high-frequency repeat imaging of an ice-covered region (Kwok et al., 2003). MR sea ice velocity fields can be used to compute spatial velocity gradients (shear, strain, vorticity, and

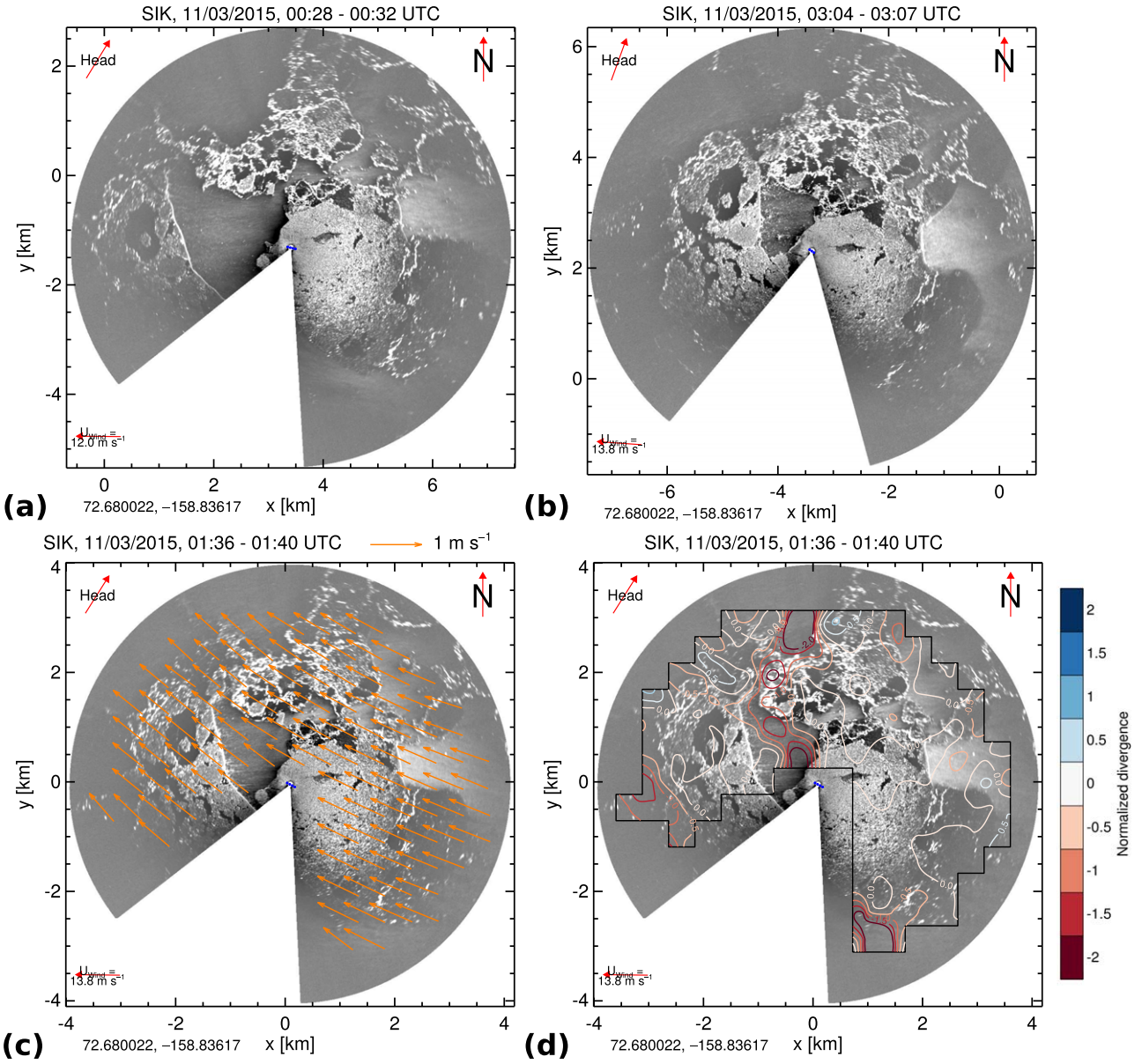

Figure 12. Example of converging sea ice drift. (a) MR sea ice image from 3 November 2015, 00:30 UTC. (b) MR sea ice image from 3 November 2015, 03:05 UTC. (c) MR sea ice image and velocity field from 3 November 2015, 01:40 UTC and (d) corresponding divergence. The divergence has been normalized by the local Coriolis frequency with contour levels ranging from −2 (dark red) to 2 (dark blue) and a contour spacing of 0.5.

divergence; Karvonen, 2013). In the following, two particularly good examples of converging and diverging sea ice drift are shown. They correspond to periods during which R/V *Sikuliaq* was moored to sea ice floes and drifting freely, allowing us to visually confirm the MR-derived divergence patterns.

Figure 12 illustrates converging sea ice drift, as observed by MR from R/V *Sikuliaq* during an ice station on 3 November 2015, from 00:30 to 03:05 UTC. The sea surface within the radar FOV was characterized by approximately equal areas of open water and first-year ice floes with a broad range of sizes (consisting of mostly snow-covered consolidated pancakes). Figures 12a and 12b show sea ice images from the beginning and end of the 2.5 h period. The large area of open water (seeded with small floes) located west of the ship shrunk considerably, indicating converging sea ice drift. Figures 12c and 12d present sea ice velocity and divergence fields from 3 November 2015, 01:38 UTC. As expected from Figures 12a and 12b, a band of convergent flow stretches from the open water area west of the ship to the northern end of the radar FOV.

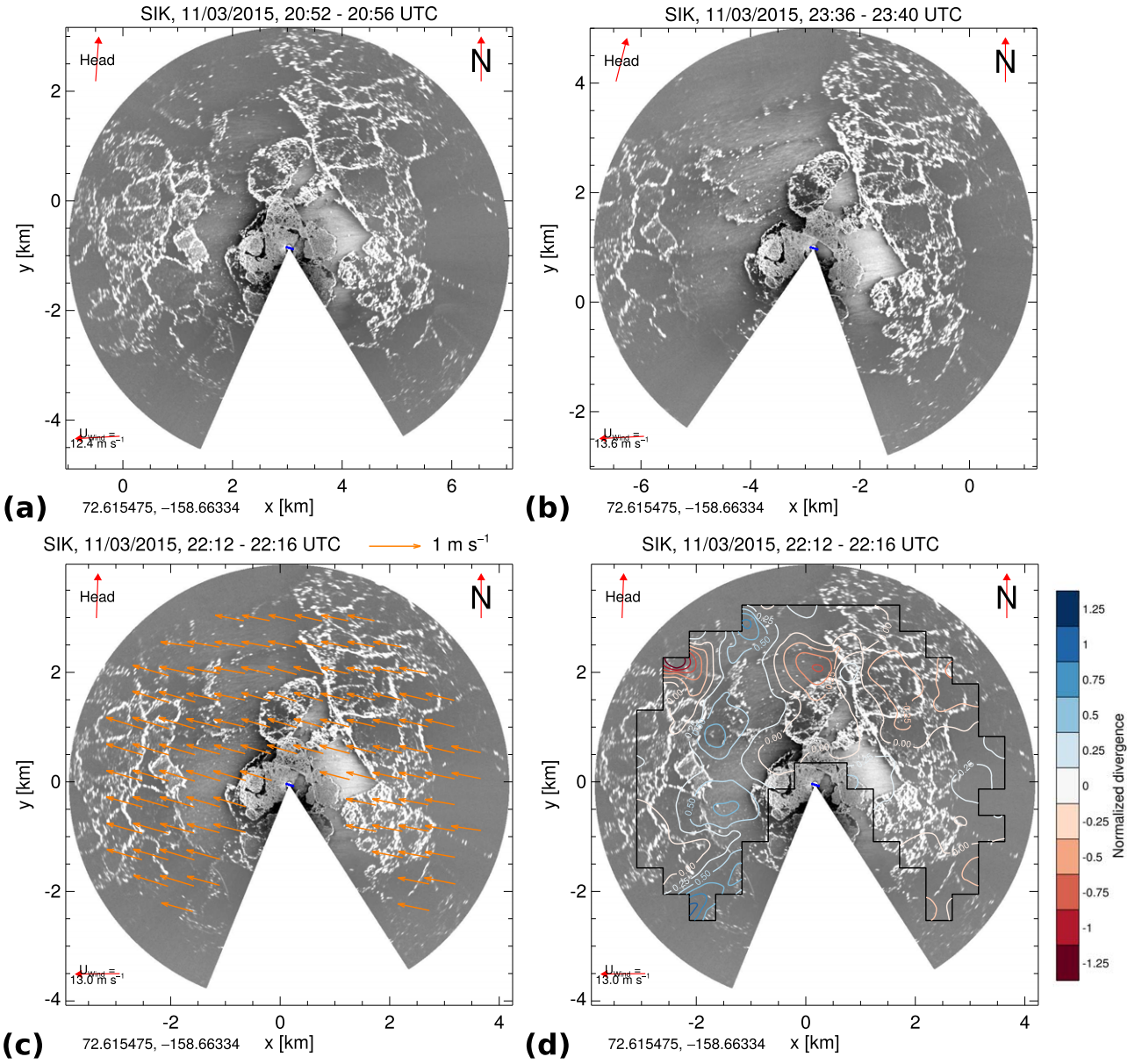

Figure 13. Example of diverging sea ice drift. (a) MR sea ice image from 3 November 2015, 20:55 UTC. (b) MR sea ice image from 3 November 2015, 23:40 UTC. (c) MR sea ice image and velocity field from 3 November 2015, 22:15 UTC and (d) corresponding divergence. The divergence has been normalized by the local Coriolis frequency with contour levels ranging from −1.25 (dark red) to 1.25 (dark blue) and a contour spacing of 0.25.

Within this band the divergence reaches minima <-2 (normalized by the local Coriolis frequency). The sea ice drift west of this band is slower with a stronger northward component than the drift on the east. The spatially averaged sea ice drift speed is 0.81 m s^{-1} with a direction of 299°.

Diverging sea ice drift was observed during another ice station on 3 November 2015, from 20:54 to 23:38 UTC. Figures 13a and 13b show sea ice images from the beginning and end of this period. A mainly open water area, west of the floe to which the ship was moored, widened significantly within the 2.75 h separating the two images. The sea ice velocity and divergence fields from 3 November 2015, 22:14 UTC, are shown in Figures 13c and 13d. The mainly open water area is characterized by divergent flow, with normalized divergence values >1. Here the sea ice drift on the western half of the radar FOV is stronger than that on the eastern one. On average, the sea ice drifts at 0.63 m s^{-1} in a direction of 284°.

5.3. Spatially Heterogeneous Drift Near Ice Edge

This subsection presents examples that are representative of the sea ice drift's spatiotemporal variability near the ice edge. (For a complete view of the MR-derived sea ice drift maps from Sea State, refer to supporting information S2.) To obtain higher quality MR sea ice imagery during periods when the ship is underway, the backscatter data are processed in "scanning" mode. This means, at any point within the radar FOV, only MR measurements (preprocessed as described in section 3.1) from the period when the ship made its closest approach are retained. As above, these data are averaged temporally to enhance the sea ice signal. To ensure sharp sea ice images despite extended averaging periods, the sea ice motion is corrected for at each pixel prior to averaging. (To this end, the relatively sparse MR sea ice velocities are interpolated linearly to cover all pixels. Areas for which there are no velocity data are filled using nearest neighbor interpolation.) The resulting composite images show sea ice features that are best defined along the ship track, where near-range measurements are available. In areas perpendicular to the ship track, for which only far-range measurements exist, the features are relatively poorly defined.

Figure 14 shows a pair of MR sea ice composite images with corresponding sea ice velocity fields. Figure 14a is based on measurements from 1 November 2015, 01:01 to 02:05 UTC, when R/V *Sikuliaq* was traveling into the pack ice. The entire radar FOV is covered by sea ice, with areas in the image's lower left quadrant blurred due to volume scattering from atmospheric ice and snow particles. The sea ice velocities were derived in continuous mode (as opposed to every 30 min as in section 5.1) using spatially fixed analysis windows. They represent temporal averages over all available measurements. Reference buoy measurements corresponding to the study period's center time are shown where available. The observed MR sea ice velocities exhibit a large degree of variability, with speeds from 0.08 to 0.56 m s^{-1} (0.29 m s^{-1} average) and directions from 289° to 54° (334° average). The mean wind was coming from 213° at 6.3 m s^{-1}. The composite image and velocity field in Figure 14b were acquired on the same day, 05:25 to 06:59 UTC, with R/V *Sikuliaq* traveling toward the ice edge. Both figures are in the same reference frame, with the (0, 0 km) location

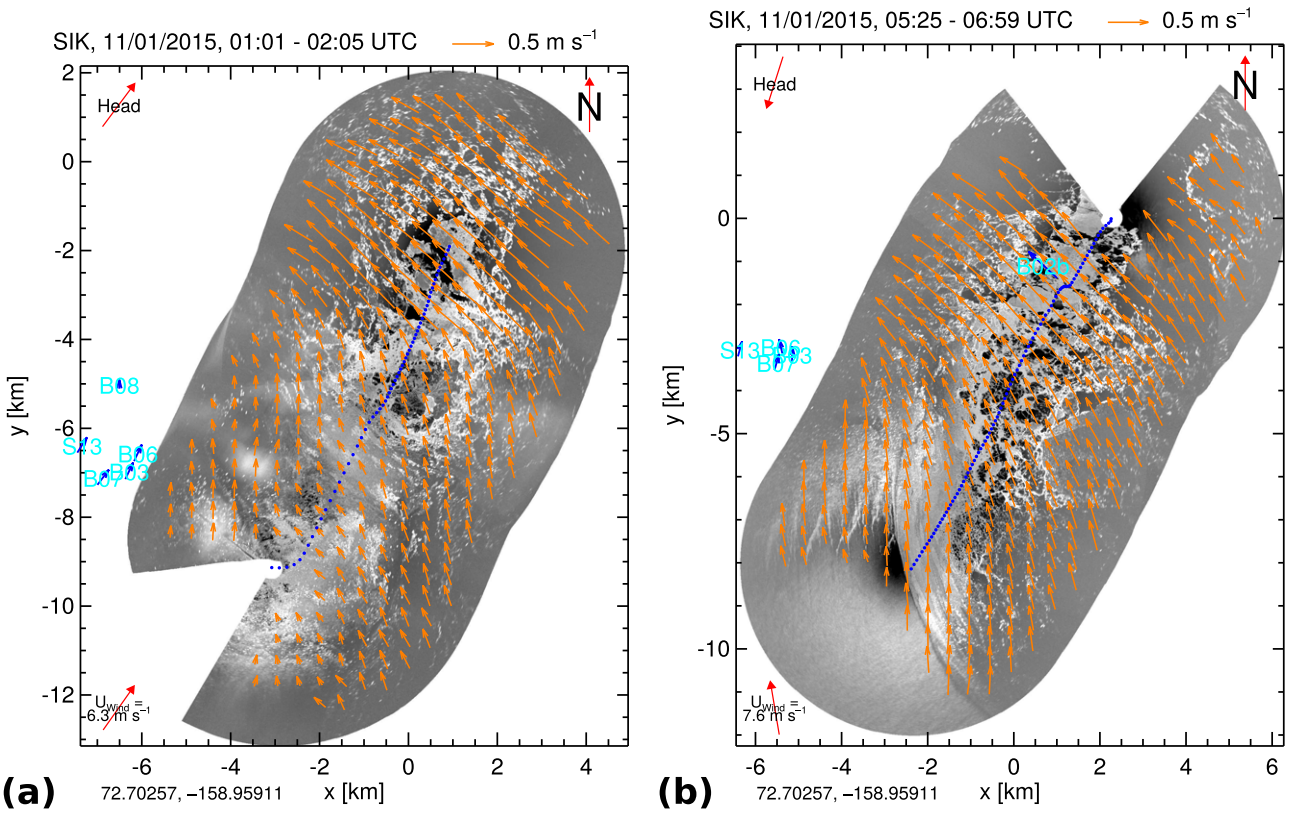

Figure 14. Sea ice velocity fields and composite sea ice images based on MR measurements from (a) 1 November 2015, 01:01 to 02:05 UTC and (b) 1 November 2015, 05:25 to 06:59 UTC. Each pixel is a 4 min average where priority is given to near-range measurements. The MR drift vectors are plotted in orange and corresponding buoy drift measurements in blue.

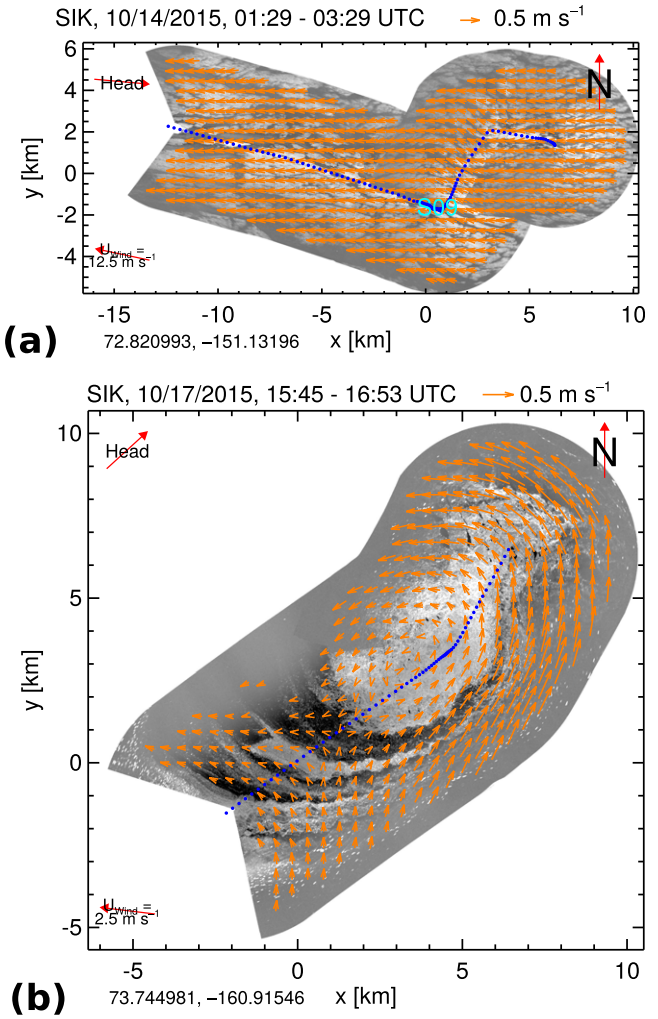

Figure 15. Sea ice velocity fields and composite sea ice images based on MR measurements from (a) 14 October 2015, 01:29 to 03:29 UTC and (b) 17 October 2015, 15:45 to 16:53 UTC. Each pixel is a 4 min average where priority is given to near-range measurements. The MR drift vectors are plotted in orange and corresponding buoy drift measurements in blue.

corresponding to −158.955° longitude and 72.703° latitude. Over the ∼5 h separating the two images, the ice edge has advanced northward and previously ice covered areas at the image's bottom have become open water. The mean sea ice and wind speeds picked up slightly, with respective average values of 0.36 and 7.6 m s^{-1}. The mean sea ice direction remained unchanged, but the mean wind direction changed to 170° (coming from). In both figures the sea ice speed increases and rotates westward from bottom to top. These results illustrate the ice edge's dynamics and the sea ice velocity field's heterogeneity over scales of 1–5 km.

The sea ice in the MIZ may take very different forms depending on the prevailing environmental conditions. Figure 15 presents example MR composite sea ice images and velocity fields from the wave event on 14 October 2015 and from the subsequent calm period on 17 October 2015. The former (Figure 15a) was characterized by strong westward winds of 12.5 m s^{-1} and waves of 2.1 m significant wave height with 6.2 s peak wave period and 314° peak wave direction. The wave parameters were measured by SWIFT buoy 09 (S09), which at the time was located inside the radar FOV. The sea ice velocity during this period was fairly uniform (standard deviations of only 0.04 m s^{-1} and 7° in speed and direction) with an average downwind (273°) drift of 0.29 m s^{-1}. The sea ice consisted of predominantly pancake and frazil ice, which, although lacking sharp-edged features, could be tracked by MR due to spatially varying densities. The MR sea ice image exhibits a few evenly spaced undulations that are mirrored by the sea ice velocity field (e.g., near S09). The latter period (Figure 15b) had weak 2.5 m s^{-1} winds in the same direction and negligible wave energy. The sea ice had a mean speed of 0.26 m s^{-1} and direction of 328° with considerably more variability (standard deviations of 0.14 m s^{-1} and 51°, respectively). During this period, the sea ice image is rich in distinct features, and includes evidence of a submesoscale (∼6 km diameter) eddy whose core is located at (4, 3.5 km). The MR sea ice velocity field confirms the presence of near-circular drift around the eddy core, however, the overall flow pattern is better described as meandering. Near the core of this submesoscale feature, the vorticity attains its minimum value of <−2 (normalized by the Coriolis frequency; see supporting information Figure S6). The SAR images in supporting information Figure S4 of the same area from 17 and 19 October further confirm the presence of eddies in the area.

6. Discussion

The shipboard MR sea ice velocity fields presented in this study have ∼500 m and up to ∼5 min resolution. Conventional satellite-derived or buoy-derived sea ice velocities do not have such fine resolution in both space and time (e.g., Kwok et al., 1998). MR therefore offers an unmatched opportunity for studying submesoscale sea ice dynamics. Here a cross-correlation-based approach for measuring sea ice drift has been proposed, which is similar to methods used in earlier sea ice drift studies (e.g., Emery et al., 1986; Karvonen et al., 2010; see section 3.2). The main reason for this choice is that it is easier to understand and more straightforward to implement than, e.g., the optical flow techniques proposed by Rohith et al. (2013) and Karvonen (2016). Others have used FFT-based phase correlation instead of cross correlation, which is less sensitive to intensity variations between image pairs (Karvonen, 2013; Kotovirta et al., 2011). This study addresses this issue by normalizing the radar images, which results in evenly distributed backscatter intensities independent of range (section 3.1). Another difference between this and previously proposed methods is that here the analysis is performed over the entire radar FOV. "Sea ice" vectors corresponding to open

water or smooth ice void of distinct radar targets are discarded through a quality control mechanism that analyzes the similarity between spatially and temporally neighboring drift estimates (section 3.3). In contrast, e.g., Karvonen (2013) first searches his MR imagery for traceable objects using an edge detection algorithm. The approach used here has the advantage that it includes the motion of ice patches with very weak backscatter, such as nilas and frazil ice. It furthermore yields a uniformly gridded velocity field, which allows the direct estimation of the sea ice field's dynamic properties (e.g., divergence and vorticity). Lastly, in SAR-based sea ice drift retrieval, where the separation time between images is on the order of hours, the cross-correlation algorithm may need to be modified to account for sea ice floe rotation (e.g., Sun, 1994). Typical rotation rates for the central Arctic pack ice and MIZ are 10^{-6} s and 10^{-5} s, respectively (Leppäranta, 2011). Given the short MR image separation time used here (75 s), ice floe rotation is negligible.

The cross-correlation-based technique assumes that the backscatter intensity within an analysis window exhibits patterns of variability that are due to the presence of sea ice and move at sea ice velocity. When applied to areas with smooth nilas ice, uniform distributions of very small ice floes (e.g., pancake ice that is significantly smaller than the 7.5 m range resolution), or open water, the cross-correlation function lacks a well-defined peak and has its maximum at a seemingly random location. The quality control removes most such cases by demanding spatiotemporal similarity. But in the rare instances where it fails, vector errors may be large. The MR backscatter from sea ice strongly depends on ice type. Distinct ice floes with significant freeboard and sharp edges (e.g., rough multiyear ice) generate a strong radar return and are likely to dominate the cross-correlation function. If such floes are embedded in ice that is barely visible to the MR (e.g., smooth nilas), the resulting drift estimate will be representative of the former, even though the two ice types may be drifting at different speeds. During the 11–14 October wave event, which is characterized by pancake ice, frazil ice, and open water, the ice-covered areas have a lower backscatter intensity than the open water. This can be explained by the fact that frazil ice dampens the cm-scale Bragg waves and inhibits wave breaking, both of which are important MR backscatter mechanisms (Brown, 1998; Trizna, 1997). But since the retrieval technique is equally sensitive to positive and negative backscatter anomalies, this fact should have no adverse effect on the results.

This study focuses on shipboard MR sea ice drift retrieval, which requires several methodological adjustments compared with earlier techniques that were designed for coastal MR stations. Most importantly, the MR measurements are georeferenced on a pulse-by-pulse basis using a highly accurate heading sensor and GPS, and calibrated to remove angular offsets in the image heading (section 3.1). Another change concerns the separation time between images, which here is significantly shorter than in, e.g., Karvonen (2013) who uses a temporal difference of 10 min. When the ship is underway (e.g., transiting at 11 kn), the short separation time ensures that sea ice velocities can be retrieved over a large area, since else sea ice features within the reference image may no longer be present in the search image (and the other way around). Another advantage of the short separation time is that computation times are reduced, since the search image size and, hence, the number of correlations increase with the separation time. The disadvantage is a relatively low velocity resolution. Here to achieve subpixel resolution, second order polynomials are least squares fitted to the cross-correlation peak and its direct neighbors (section 3.2).

How accurate is the proposed shipboard MR sea ice velocity field retrieval? The RMS errors from the MR-R/V *Sikuliaq*, MR-SWIFT, and MR-wave buoy comparisons of sea ice velocity components range from $\sim$1 to 6 cm s^{-1} (see Table 1 in section 4). The MR-R/V *Sikuliaq* comparison yields best results (RMS errors of 0.75 and 0.77 cm s^{-1} for u and v, respectively) and is based on the largest number of data points (255). However, it is important to note that this comparison eliminates any errors that are due to the shipboard GPS, since the GPS signal that is used to compute the reference sea ice velocity, is at the same time used for the georeferencing of the MR backscatter intensity measurements (section 3.1). The Seapath multi-antenna GPS receiver offers 1 m position accuracy. A 1 m error over the 75 s separation time between images corresponds to a speed of 1.33 cm s^{-1}. But since 1–3 min worth of GPS measurements contribute to each image (depending on the averaging period), this error should be reduced by averaging. The MR-SWIFT and MR-wave buoy comparisons include errors from both the shipboard and buoy GPS receivers, which explains some of the observed differences. Another possible source of MR-buoy differences stems from the fact that neither SWIFT nor wave buoys were designed to drift with the sea ice or water they are deployed in. From modern drifter design, it is well documented that the passage of waves through a drifter (or buoy) may add an artificial velocity (e.g., Novelli et al., 2017). Since the MR-buoy sea ice velocity pairs stem from periods when

surface waves were present, wave rectification likely explains additional MR-buoy differences. While the available data do not permit a definite answer, it could be that the bulkier design of the wave buoys enhances wave rectification motions, which would explain the higher RMS errors for the MR-wave buoy comparison (5.65 and 3.33 cm s^{-1} for u and v, respectively) relative to the MR-SWIFT comparison (2.96 and 2.75 cm s^{-1}). To conclude, the shipboard MR sea ice velocities derived by the method proposed here likely have an accuracy of 1–3 cm s^{-1}.

Mahoney et al. (2015), who use an optical flow approach to derive sea ice velocities from coastal MR data, which they compare against ADCP bottom-tracked sea ice velocities, report sea ice speed RMS errors of 12–24 cm s^{-1} (after reducing the high-frequency scatter in their MR sea ice speeds through the use of a 2 h median filter). These significantly larger errors can be explained by differences in the MR sea ice velocity retrieval methods, the relatively low range resolution (21.5 m) of their radar (or, possibly, low sampling frequency of their radar input card), the fact that their MR images are recorded only every 4 min and without temporal averaging, which would enhance the sea ice signal, uncertainties in the time stamps of their MR images, and the ADCP's 5 km distance from the radar transceiver.

The sea ice motions observed by shipboard MR during the Sea State field experiment in the Beaufort Sea's fall MIZ exhibit large spatiotemporal gradients, especially near the ice edge. In particular, this study observed distinct near-inertial oscillations, converging and diverging motions, as well as active submesoscales, including a remarkable eddying or meandering flow. Previous studies have used satellite images to document the existence of mesoscale eddies in the Arctic (Johannessen et al., 1987a, 1987b). Beyond providing eddy size and location, the data on which these studies were based do not allow a more quantitative analysis. Numerical model studies of the MIZ show that baroclinic instabilities associated with horizontal buoyancy gradients, caused by wind-induced upwelling/downwelling or meltwater fronts, may result in the generation of strong currents and eddies (Häkkinen, 1986; Lu et al., 2015). To the authors best knowledge, the MR sea ice velocity field shown in Figure 15b allowed the first description of the dynamic properties of a small-scale eddy or meander in the Arctic.

The relatively low correlation between sea ice and wind speed ($r^2 = 0.34$) suggests that ocean currents contribute heavily to the observed drift. For comparison, during the SHEBA drift in the western Arctic the GPS-tracked sea ice and wind speed had a much higher correlation of $r^2 = 0.83$ (Persson, 2011). What is more, the observed sea ice velocities exhibit uncharacteristically large surface wind factors (3.5–5%). Several recent studies support these findings. Rampal et al. (2009) and McPhee (2012) observed an increasing mean sea ice speed and deformation rate in the Arctic, which they attribute to an enhanced mobility resulting from climate change related reductions in sea ice thickness and concentration. Gimbert et al. (2012) explain their observations of strengthening inertial oscillations in recent years with the weakening pack ice. Similarly, Manucharyan and Thompson (2017) argue that the coupling between sea ice drift and submesoscale ocean currents is becoming more important, since Arctic climate change is accompanied by an increase in the MIZ's areal content. Lastly, the proximity to the shelf break and its associated eddies may have further contributed to the strong sea ice velocities observed in this study (D'Asaro, 1988).

Mahoney et al. (2007) have used coastal MR-derived sea ice velocities to estimate the ocean current underneath, assuming a drag coefficient for rough landfast ice from the literature, and neglecting wind contributions. Here wind drag is not negligible. Nevertheless, combined shipborne air, sea, and ice drift data could yield valuable sea ice information. The shipboard ADCP measurements made during Sea State are unfortunately too noisy to yield reliable upper ocean currents. This may be due to a shortage of ocean acoustic scatterers, on which the ADCP current measurements depend. In the future, under free drift conditions (i.e., zero sea ice internal stress), as typically encountered in the MIZ (Leppäranta, 2011), it will be worthwhile to use sea ice velocity, wind drag, and upper ocean current measurements to estimate the drag at the ice-ocean interface.

7. Conclusions

This study is based on MR measurements from R/V *Sikuliaq* that were collected during the Sea State field experiment in the Beaufort Sea's fall MIZ. Previous studies have successfully used data from coastal or drifting MR stations to measure sea ice motion (e.g., Karvonen, 2016; Rohith et al., 2013). To accurately retrieve sea ice drift from a ship, the MR measurements must be georeferenced, using a highly accurate position

and heading sensor, and calibrated to remove offsets in the MR image heading (Lund et al., 2015; McCann & Bell, 2018). Sea ice velocity fields are derived by cross correlating pairs of temporally averaged and normalized MR sea ice images that are separated by a short (75 s) period. The resulting sea ice velocity fields have ~500 m and up to ~5 min resolution. A similarity-based quality control separates sea ice drift from open water and other measurements lacking a sea ice signal. The sea ice drift retrieval technique has been applied to the entire (~4 weeks) set of Sea State MR data. During one energetic wave event, the sea ice signal risked being overshadowed by surface wave signatures. An extended averaging period coupled with a novel sea ice drift correction ensured accurate sea ice drift estimates under these adverse conditions. The MR sea ice velocities were validated using independent drift measurements from buoys and R/V *Sikuliaq* during ice stations. The MR and reference sea ice velocities are in excellent agreement, with RMS errors ranging from 0.8 to 5.6 cm s^{-1}. The only other published independent validation of MR sea ice velocities from a coastal station yielded RMS speed errors of 12–24 cm s^{-1} (Mahoney et al., 2015).

The MR sea ice velocities correlate weakly with the shipborne wind speeds ($r^2 = 0.34$), which marks a departure from our current understanding of mainly wind-driven sea ice drift. They furthermore exhibit a large degree of spatiotemporal variability. These findings suggest that submesoscale ocean currents, e.g., resulting from horizontal buoyancy gradients due to upwelling or melt (Häkkinen, 1986; Lu et al., 2015), played an important role in forcing the observed sea ice motion. Several examples presented here corroborate this interpretation, showing highly variable flow patterns near the ice edge, converging and diverging sea ice motions (normalized divergences <-2 and >1), as well as a small-scale eddy or meander (normalized vorticity <-2). The lowest wind-ice speed correlations were observed in proximity to the ice edge (ice concentrations $<50\%$). The sea ice reached maximum speeds >1 m s^{-1}. The average speed factor and turning angle are 5.0% and $+18°$ (to the right of the wind direction), respectively. The former value is significantly larger than the typical 2% that have been reported for the Arctic (Leppäranta, 2011).

Recent research indicates that submesoscale ocean currents will be strengthening as the Arctic ice cover recedes and thins (Vihma et al., 2014). However, Manucharyan and Thompson (2017) find that the heat flux parameterizations used by current climate models do not sufficiently account for submesoscale motions. Routine shipboard MR sea ice velocity measurements can provide new insights into the small-scale dynamic properties of sea ice, which conventional measurement techniques are typically unable to resolve. They can also be used to improve our understanding of air-sea-ice interaction processes and sea ice modeling. The authors are presently working on combining the MR sea ice velocity data with MR-derived near-surface current fields, which require the presence of a surface wave signal (Lund et al., 2018), and shipboard wind stress measurements to estimate the ocean drag as a momentum budget residual. If carried out in near-real time, which could be accomplished easily with a state-of-the-art personal computer, MR sea ice velocity fields could also be used to aid ship routing decisions or risk assessment during on-ice operations.

As a by-product of the sea ice drift retrieval, this study proposes a novel sea ice imaging method that corrects for sea ice drift (as well as ship motion), allowing extended averaging periods. The resulting sea ice images lack the characteristic speckle noise due to the large number of data points at each image resolution cell, and features remain clear as a result of the drift correction. This method could prove valuable for science and ship operations, e.g., it could help detect drifting buoys or hazardous bergy bits and growlers with small radar cross sections. (During Sea State, the Rutter system, which allows scan averaging, but does not account for sea ice drift, enabled the recovery of several wave buoys which had stopped transmitting their positions due to heavy icing.) For periods during which the ship is underway, the authors propose a "scanning" mode which favors near-range over far-range measurements. The resulting composite sea ice images present an excellent starting point for the MR-based estimation of the open water percentage, floe size distribution, and, possibly, sea ice classification, which are topics for future study.

Acknowledgments
The authors appreciate the valuable feedback from Andy Mahoney and one anonymous reviewer, whose insights and expertise helped improve this manuscript significantly. B.L. and H.C.G. acknowledge funding by the US Office of Naval Research (grants N00014-13-1–0288 and N00014–15-1–2638). The crew of R/V *Sikuliaq* provided excellent support throughout the field experiment. A time series covering the entire field experiment and including the composite wind velocity, quality-controlled and spatially averaged MR sea ice velocity, as well as sea ice parameters can be found at http://www.apl.uw.edu/arcticseastate.

References

Andreas, E. L., Tucker, W. B., & Ackley, S. F. (1984). Atmospheric boundary-layer modification, drag coefficient, and surface heat flux in the Antarctic marginal ice zone. *Journal of Geophysical Research*, *89*(C1), 649–661.

Beitsch, A., Kaleschke, L., & Kern, S. (2014). Investigating high-resolution AMSR2 sea ice concentrations during the February 2013 fracture event in the Beaufort Sea. *Remote Sensing*, *6*(5), 3841–3856.

Bouillon, S., & Rampal, P. (2015). On producing sea ice deformation data sets from SAR-derived sea ice motion. *The Cryosphere*, *9*(2), 663–673.

Brown, G. S. (1998). Guest Editorial—Special issue on low-grazing-angle backscatter from rough surfaces. *IEEE Transactions on Antennas and Propagation*, *46*(1), 1–2.
Campbell, W., Weeks, W., Ramseier, R., & Gloersen, P. (1975). Geophysical studies of floating ice by remote sensing. *Journal of Glaciology*, *15*(73), 305–328.
Campbell, W. J. (1965). The wind-driven circulation of ice and water in a polar ocean. *Journal of Geophysical Research*, *70*(14), 3279–3301.
Cheng, S., Rogers, W., Thomson, E., Smith, J., Doble, M., Wadhams, M. P., et al. (2017). Calibrating a viscoelastic sea ice model for wave propagation in the Arctic fall marginal ice zone. *Journal of Geophysical Research: Oceans*, *122*, 8770–8793. https://doi.org/10.1002/2017JC013275
Collins, C. O., III, Blomquist, B., Persson, O., Lund, B., Rogers, W. E., Thomson, J., et al. (2017). Doppler correction of wave frequency-spectra measured by underway vessels. *Journal of Atmospheric and Oceanic Technology*, *34*(2), 429–436.
Curlander, J., Holt, B., & Hussey, K. (1985). Determination of sea ice motion using digital SAR imagery. *IEEE Journal of Oceanic Engineering*, *10*(4), 358–367.
D'Asaro, E. A. (1988). Generation of submesoscale vortices: A new mechanism. *Journal of Geophysical Research*, *93*(C6), 6685–6693.
Druckenmiller, M. L., Eicken, H., Johnson, M. A., Pringle, D. J., & Williams, C. C. (2009). Toward an integrated coastal sea-ice observatory: System components and a case study at Barrow, Alaska. *Cold Regions Science and Technology*, *56*, 61–72.
Emery, W. J., Fowler, C. W., & Maslanik, J. A. (1997). Satellite-derived maps of Arctic and Antarctic sea ice motion: 1988 to 1994. *Geophysical Research Letters*, *24*(8), 897–900.
Emery, W. J., Thomas, A. C., Collins, M. J., Crawford, W. R., & Mackas, D. L. (1986). An objective method for computing advective surface velocities from sequential infrared satellite images. *Journal of Geophysical Research*, *91*(C11), 12865–12878.
Fily, M., & Rothrock, D. A. (1987). Sea ice tracking by nested correlations. *IEEE Transactions on Geoscience and Remote Sensing*, *GE-25*(5), 570–580.
Flock, W. (1977). Monitoring open water and sea ice in the Bering Strait by radar. *IEEE Transactions on Geoscience Electronics*, *15*(4), 196–202.
Gimbert, F., Marsan, D., Weiss, J., Jourdain, N. C., & Barnier, B. (2012). Sea ice inertial oscillations in the Arctic Basin. *The Cryosphere*, *6*, 1187–1201.
Girard-Ardhuin, F., & Ezraty, R. (2012). Enhanced Arctic sea ice drift estimation merging radiometer and scatterometer data. *IEEE Transactions on Geoscience and Remote Sensing*, *50*(7), 2639–2648.
Gommenginger, C. P., Ward, N. P., Fisher, G. J., Robinson, I. S., & Boxall, S. R. (2000). Quantitative microwave backscatter measurements from the ocean surface using digital marine radar images. *Journal of Atmospheric and Oceanic Technology*, *17*(5), 665–678.
Grumbine, R. W. (1998). Virtual floe ice drift forecast model intercomparison. *Weather and Forecasting*, *13*(3), 886–890.
Haapala, J., Lönnroth, N., & Stössel, A. (2005). A numerical study of open water formation in sea ice. *Journal of Geophysical Research*, *110*, C09011. https://doi.org/10.1029/2003JC002200
Haarpaintner, J. (2006). Arctic-wide operational sea ice drift from enhanced-resolution QuikScat/SeaWinds scatterometry and its validation. *IEEE Transactions on Geoscience and Remote Sensing*, *44*(1), 102–107.
Häkkinen, S. (1986). Coupled ice-ocean dynamics in the marginal ice zones: Upwelling/downwelling and eddy generation. *Journal of Geophysical Research*, *91*(C1), 819–832.
Hall, R. T., & Rothrock, D. A. (1981). Sea ice displacement from Seasat synthetic aperture radar. *Journal of Geophysical Research*, *86*(C11), 11078–11082.
Haykin, S., Currie, B., Lewis, E., & Nickerson, K. (1985). Surface-based radar imaging of sea ice. *Proceedings of the IEEE*, *73*(2), 233–251.
Haykin, S., Lewis, E., Raney, R., & Rossiter, J. (1994). *Remote sensing of sea ice and icebergs, Wiley series in remote sensing*. New York, NY: John Wiley.
Heil, P., & Hibler, W. D., III (2002). Modeling the high-frequency component of Arctic sea ice drift and deformation. *Journal of Physical Oceanography*, *32*(11), 3039–3057.
Holloway, G., & Proshutinsky, A. (2007). Role of tides in Arctic ocean/ice climate. *Journal of Geophysical Research*, *112*, C04S06. https://doi.org/10.1029/2006JC003643
Holt, B., Rothrock, D. A., & Kwok, R. (1992). *Determination of sea ice motion from satellite images* (pp. 343–354). Washington, DC: American Geophysical Union.
Hutchings, J. K., & Hibler, W. D. (2008). Small-scale sea ice deformation in the Beaufort Sea seasonal ice zone. *Journal of Geophysical Research*, *113*, C08032. https://doi.org/10.1029/2006JC003971
Jernelöv, A. (2010). The threats from oil spills: Now, then, and in the future. *AMBIO: A Journal of the Human Environment*, *39*(6), 353–366.
Johannessen, J., O., Johannessen, E., Svendsen, R., Shuchman, T., Manley, W., Campbell, E., et al. (1987a). Mesoscale eddies in the Fram Strait marginal ice zone during the 1983 and 1984 Marginal Ice Zone Experiments. *Journal of Geophysical Research*, *92*(C7), 6754–6772.
Johannessen, O., Johannessen, J., Svendsen, E., Shuchman, R., Campbell, W., & Josberger, E. (1987b). Ice-edge eddies in the Fram Strait marginal ice zone. *Science*, *236*(4800), 427–429.
Karvonen, J. (2012). Operational SAR-based sea ice drift monitoring over the Baltic Sea. *Ocean Science*, *8*(4), 473–483.
Karvonen, J. (2013). Tracking the motion of recognizable sea-ice objects from coastal radar image sequences. *Annals of Glaciology*, *54*(62), 41–49.
Karvonen, J. (2016). Virtual radar ice buoys—A method for measuring fine-scale sea ice drift. *The Cryosphere*, *10*(1), 29–42.
Karvonen, J., Heiler, I., & Haapala, J. (2010). *Ice drift information retrieval from radar time series*. Paper presented at the Proceedings of the 20th IAHR International Symposium on Ice, Lahti, Finland, June 14–18, 2010.
Khon, V. C., Mokhov, I. I., Latif, M., Semenov, V. A., & Park, W. (2010). Perspectives of Northern Sea Route and Northwest Passage in the twenty-first century. *Climatic Change*, *100*(3), 757–768.
Kotovirta, V., Karvonen, J., von Bock und Polach, R., Berglund, R., & Kujala, P. (2011). Ships as a sensor network to observe ice field properties. *Cold Regions Science and Technology*, *65*(3), 359–371.
Kwok, R. (1998). The RADARSAT geophysical processor system. In *Analysis of SAR data of the polar oceans: Recent Advances* (pp. 235–257).
Kwok, R. (2006). Contrasts in sea ice deformation and production in the Arctic seasonal and perennial ice zones. *Journal of Geophysical Research*, *111*, C11S22. https://doi.org/10.1029/2005JC003246
Kwok, R. (2010). Satellite remote sensing of sea-ice thickness and kinematics: A review. *Journal of Glaciology*, *56*(200), 1129–1140.
Kwok, R., Cunningham, G. F., & Hibler, W. D. (2003). Sub-daily sea ice motion and deformation from RADARSAT observations. *Geophysical Research Letters*, *30*(23), 2218. https://doi.org/10.1029/2003GL018723
Kwok, R., Curlander, J. C., McConnell, R., & Pang, S. S. (1990). An ice-motion tracking system at the Alaska SAR facility. *IEEE Journal of Oceanic Engineering*, *15*(1), 44–54.

Kwok, R., Schweiger, A., Rothrock, D., Pang, S., & Kottmeier, C. (1998). Sea ice motion from satellite passive microwave imagery assessed with ERS SAR and buoy motions. *Journal of Geophysical Research*, *103*(C4), 8191–8214.
Kwok, R., Spreen, G., & Pang, S. (2013). Arctic sea ice circulation and drift speed: Decadal trends and ocean currents. *Journal of Geophysical Research: Oceans*, *118*, 2408–2425. https://doi.org/10.1002/jgrc.20191
Ledley, T. S. (1988). A coupled energy balance climate-sea ice model: Impact of sea ice and leads on climate. *Journal of Geophysical Research*, *93*(D12), 15919–15932.
Leppäranta, M. (2011). *The drift of sea ice*. Berlin, Germany: Springer Science & Business Media.
Lewis, E., Currie, B., & Haykin, S. (1994). Remote sensing of sea-ice and icebergs. In *Surface-based radar: Noncoherent* (Chap. 8, pp. 341–442). New York, NY: John Wiley.
Lindsay, R. W., & Stern, H. L. (2003). The RADARSAT geophysical processor system: Quality of sea ice trajectory and deformation estimates. *Journal of Atmospheric and Oceanic Technology*, *20*(9), 1333–1347.
Lu, K., Weingartner, T., Danielson, S., Winsor, P., Dobbins, E., Martini, K., et al. (2015). Lateral mixing across ice meltwater fronts of the Chukchi Sea shelf. *Geophysical Research Letters*, *42*, 6754–6761. https://doi.org/10.1002/2015GL064967
Lu, P., Li, Z., Shi, L., & Huang, W. (2013). Marine radar observations of iceberg distribution in the summer Southern Ocean. *Annals of Glaciology*, *54*(62), 35–40.
Lund, B., Graber, H. C., Hessner, K., & Williams, N. J. (2015). On shipboard marine X-band radar near-surface current "calibration." *Journal of Atmospheric and Oceanic Technology*, *32*(10), 1928–1944.
Lund, B., Graber, H. C., & Romeiser, R. (2012). Wind retrieval from shipborne nautical X-band radar data. *IEEE Transactions on Geoscience and Remote Sensing*, *50*(10), 3800–3811.
Lund, B., Haus, B., Horstmann, K. J., Graber, H., Carrasco, C. R., Laxague, N. J., et al. (2018). Near-surface current mapping by shipboard marine X-band radar: A validation. *Journal of Atmospheric and Oceanic Technology*, *35*, 1077–1090. https://doi.org/10.1175/JTECH-D-17-0154.1
Lund, B., Zappa, C. J., Graber, H. C., & Cifuentes-Lorenzen, A. (2017). Shipboard wave measurements in the Southern Ocean. *Journal of Atmospheric and Oceanic Technology*, *34*(9), 2113–2126.
Mahoney, A., Eicken, H., & Shapiro, L. (2007). How fast is landfast sea ice? A study of the attachment and detachment of nearshore ice at Barrow, Alaska. *Cold Regions Science and Technology*, *47*(3), 233–255.
Mahoney, A. R., Eicken, H., Fukamachi, Y., Ohshima, K. I., Simizu, D., Kambhamettu, C., et al. (2015). Taking a look at both sides of the ice: Comparison of ice thickness and drift speed as observed from moored, airborne and shore-based instruments near Barrow, Alaska. *Annals of Glaciology*, *56*(69), 363–372.
Manucharyan, G. E., & Thompson, A. F. (2017). Submesoscale sea ice-ocean interactions in marginal ice zones. *Journal of Geophysical Research: Oceans*, *122*, 9455–9475. https://doi.org/10.1002/2017JC012895
Martinson, D. G., & Wamser, C. (1990). Ice drift and momentum exchange in winter Antarctic pack ice. *Journal of Geophysical Research*, *95*(C2), 1741–1755.
McCann, D. L., & Bell, P. S. (2018). A simple offset "calibration" method for the accurate geographic registration of ship-borne X-band radar intensity imagery. *IEEE Access*, *6*, 13939–13948.
McPhee, M. G. (1980). An analysis of pack ice drift in summer. In Sea *ice processes and models* (pp. 62–75).
McPhee, M. G. (2012). Advances in understanding ice–ocean stress during and since AIDJEX. *Cold Regions Science and Technology*, *76*(Suppl. C), 24–36.
McPhee, M. G., Maykut, G. A., & Morison, J. H. (1987). Dynamics and thermodynamics of the ice/upper ocean system in the marginal ice zone of the Greenland Sea. *Journal of Geophysical Research*, *92*(C7), 7017–7031.
Nansen, F. (1902). The oceanography of the North Polar Basin. The Norwegian North Polar Expedition 1893–1896. *Scientific Results*, *3*(9).
Ninnis, R. M., Emery, W. J., & Collins, M. J. (1986). Automated extraction of pack ice motion from advanced very high resolution radiometer imagery. *Journal of Geophysical Research*, *91*(C9), 10725–10734.
Novelli, G., Guigand, C. M., Cousin, C., Ryan, E. H., Laxague, N. J., Dai, H., et al. (2017). A biodegradable surface drifter for ocean sampling on a massive scale. *Journal of Atmospheric and Oceanic Technology*, *34*(11), 2509–2532.
Nye, J. (1975). The use of ERTS photographs to measure the movement and deformation of sea ice. *Journal of Glaciology*, *15*(73), 429–436.
O'Connell, B. (2008). *Marine radar for improved ice detection*. Paper presented at the Proceedings of the 8th International Conference on Ships and Marine Structures in Ice (ICETECH 2008).
Padman, L., & Kottmeier, C. (2000). High-frequency ice motion and divergence in the Weddell Sea. *Journal of Geophysical Research*, *105*(C2), 3379–3400.
Parsa, A. (2013a). *Ice age classification using cross-polarization measurement with X-band radar*. Paper presented at the Twenty-Third International Offshore and Polar Engineering Conference, International Society of Offshore and Polar Engineers.
Parsa, A. (2013b). Surface roughness observation of arctic ice using low grazing angle radar. In *Radar Conference (RADAR), 2013 IEEE* (pp. 1–5). Piscataway, NJ: IEEE.
Perrette, M., Yool, A., Quartly, G., & Popova, E. (2011). Near-ubiquity of ice-edge blooms in the Arctic. *Biogeosciences*, *8*(2), 515.
Persson, P. O. G. (2011). *Relative roles of wind forcing and ice dynamics for predicting short-term sea-ice movement as estimated from in-situ observations*. Paper presented at the World Climate Research Programme Open Science Conference.
Persson, P. O. G., Blomquist, B., Guest, P., Stammerjohn, S., Fairall, C., Rainville, L., et al. (2018). Shipboard observations of the meteorology and near-surface environment during autumn freeze-up in the Beaufort/Chukchi Seas. *Journal of Geophysical Research: Oceans*, *123*. https://doi.org/2018JC013786
Ponter, A., Palmer, A., Goodman, D., Ashby, M., Evans, A., & Hutchinson, J. (1983). The force exerted by a moving ice sheet on an offshore structure: Part 1. The creep mode. *Cold Regions Science and Technology*, *8*(2), 109–118.
Rampal, P., Weiss, J., & Marsan, D. (2009). Positive trend in the mean speed and deformation rate of Arctic sea ice, 1979–2007. *Journal of Geophysical Research*, *114*, C05013. https://doi.org/10.1029/2008JC005066
Rogers, W. E., Thomson, J., Shen, H. H., Doble, M. J., Wadhams, P., & Cheng, S. (2016). Dissipation of wind waves by pancake and frazil ice in the autumn Beaufort Sea. *Journal of Geophysical Research: Oceans*, *121*, 7991–8007. https://doi.org/10.1002/2016JC012251
Rohith, M. V., Jones, J., Eicken, H., & Kambhamettu, C. (2013). Extracting quantitative information on coastal ice dynamics and ice hazard events from marine radar digital imagery. *IEEE Transactions on Geoscience and Remote Sensing*, *51*(5), 1–15.
Rousset, C., Vancoppenolle, M., Madec, G., Fichefet, T., Flavoni, S., Barthélemy, A., et al. (2015). The Louvain-La-Neuve sea ice model LIM3.6: Global and regional capabilities. *Geoscientific Model Development*, *8*(10), 2991–3005.
Schweiger, A. J., & Zhang, J. (2015). Accuracy of short-term sea ice drift forecasts using a coupled ice-ocean model. *Journal of Geophysical Research: Oceans*, *120*, 7827–7841. https://doi.org/10.1002/2015JC011273

Shapiro, L. H., & Metzner, R. C. (1989). *Nearshore ice conditions from radar data, Point Barrow area, Alaska*. Fairbanks: Geophysical Institute, University of Alaska.
Shirasawa, K., Ebuchi, N., Leppäranta, M., & Takatsuka, T. (2013). Ice-edge detection from Japanese C-band radar and high-frequency radar coastal stations. *Annals of Glaciology*, *54*(62), 59–64.
Skiles, F. L. (1968). Empirical wind drift of sea ice. In *Arctic drifting stations* (pp. 239–252).
Smith, M., Stammerjohn, S., Persson, O., Rainville, L., Liu, G., Perrie, W., et al. (2018). Episodic reversal of autumn ice advance caused by release of ocean heat in the Beaufort Sea. *Journal of Geophysical Research: Oceans*, *123*. https://doi.org/10.1002/2018JC013764
Smith, S. D., Muench, R. D., & Pease, C. H. (1990). Polynyas and leads: An overview of physical processes and environment. *Journal of Geophysical Research*, *95*(C6), 9461–9479.
Spreen, G., Kaleschke, L., & Heygster, G. (2008). Sea ice remote sensing using AMSR-E 89-GHz channels. *Journal of Geophysical Research*, *113*, C02S03. https://doi.org/10.1029/2005JC003384
Squire, V. A. (2007). Of ocean waves and sea-ice revisited. *Cold Regions Science and Technology*, *49*(2), 110–133.
Stopa, J. E., Ardhuin, F., & Girard-Ardhuin, F. (2016). Wave climate in the Arctic 1992–2014: Seasonality and trends. *The Cryosphere*, *10*(4), 1605–1629.
Sumata, H., Lavergne, T., Girard-Ardhuin, F., Kimura, N., Tschudi, M. A., Kauker, F., et al. (2014). An intercomparison of Arctic ice drift products to deduce uncertainty estimates. *Journal of Geophysical Research: Oceans*, *119*, 4887–4921. https://doi.org/10.1002/2013JC009724
Sun, Y. (1994). A new correlation technique for ice-motion analysis. *EARSeL International Journal Advances in Remote Sensing*, *3*(2), 57–63.
Tabata, T. (1975). Sea-ice reconnaissance by radar. *Journal of Glaciology*, *15*(73), 215–224.
Tabata, T., Kawamura, T., & Aota, M. (1980). Divergence and rotation of an ice field off Okhotsk Sea Coast of Hokkaido. In *Sea ice processes and models* (Vol. 98195). Seattle, WA: University of Washington Press.
Thomas, M., Geiger, C., & Kambhamettu, C. (2008). High resolution (400 m) motion characterization of sea ice using ERS-1 SAR imagery. *Cold Regions Science and Technology*, *52*(2), 207–223.
Thomson, J. (2012). Wave breaking dissipation observed with "SWIFT" drifters. *Journal of Atmospheric and Oceanic Technology*, *29*(12), 1866–1882.
Thomson, J. (2015). *ONR Sea State DRI Cruise Report: R/V Sikuliaq, Fall 2015* (Rep. SKQ201512S). Seattle: University of Washington.
Thomson, J., Ackley, F., Girard-Ardhuin, S., Ardhuin, F., Brozena, J., Cheng, S., et al. (2018), Overview of the Arctic Sea State and Boundary Layer Physics Program. *Journal of Geophysical Research: Oceans*, *123*. https://doi.org/10.1002/2018JC013766
Thomson, J., Fan, Y., Stammerjohn, S., Stopa, J., Rogers, W. E., Girard-Ardhuin, F., et al. (2016). Emerging trends in the sea state of the Beaufort and Chukchi seas. *Ocean Modelling*, *105*, 1–12.
Thorndike, A., Rothrock, D., Maykut, G., & Colony, R. (1975). The thickness distribution of sea ice. *Journal of Geophysical Research*, *80*(33), 4501–4513.
Thorndike, A. S., & Colony, R. (1982). Sea ice motion in response to geostrophic winds. *Journal of Geophysical Research*, *87*(C8), 5845–5852.
Timmermans, M.-L., Cole, S., & Toole, J. (2012). Horizontal density structure and restratification of the Arctic ocean surface layer. *Journal of Physical Oceanography*, *42*(4), 659–668.
Trizna, D. B. (1997). A model for Brewster angle damping and multipath effects on the microwave radar sea echo at low grazing angles. *IEEE Transactions on Geoscience and Remote Sensing*, *35*(5), 1232–1244.
Vesecky, J. F., Samadani, R., Smith, M. P., Daida, J. M., & Bracewell, R. N. (1988). Observation of sea-ice dynamics using synthetic aperture radar images: Automated analysis. *IEEE Transactions on Geoscience and Remote Sensing*, *26*(1), 38–48.
Vihma, T., R., Pirazzini, I., Fer, I. A., Renfrew, J., Sedlar, M., Tjernström, C., et al. (2014). Advances in understanding and parameterization of small-scale physical processes in the marine Arctic climate system: A review. *Atmospheric Chemistry and Physics*, *14*(17), 9403–9450.
Wadhams, P. (1980). Ice characteristics in the seasonal sea ice zone. *Cold Regions Science and Technology*, *2*(Suppl. C), 38–87.
Wadhams, P., & Thomson, J. (2015). The Arctic Ocean cruise of R/V Sikuliaq 2015, an investigation of waves and the advancing ice edge. *Il Polo*, *70*(4), 9–38.
Weatherall, P., Marks, K. M., Jakobsson, M., Schmitt, T., Tani, S., Arndt, J. E., et al. (2015). A new digital bathymetric model of the world's oceans. *Earth and Space Science*, *2*(8), 331–345.